Closed-channel block of BK potassium channels by bbTBA requires partial activation

Qiong-Yao Tang, Xu-Hui Zeng, and Christopher J. Lingle

Department of Anesthesiology, Washington University School of Medicine, St. Louis, MO 63110

Blockade of large-conductance Ca^{2+}-activated K^+ (BK) channels by the bulky quaternary ammonium compound, *N*-(4-[benzoyl]benzyl)-*N,N,N*-tributylammonium (bbTBA), exhibits features consistent with blockade of both closed and open states. Here, we examine block of closed BK channels by bbTBA and how it may differ from block of open channels. Although our observations generally confirm earlier results, we describe three observations that are inconsistent with a model in which closed and open channels are equally accessible to blockade by bbTBA. First, block by bbTBA exhibits Ca^{2+}-dependent features that are inconsistent with strictly state-independent block. Second, the steady-state voltage dependence of bbTBA block at negative potentials shows that any block of completely closed states either does not occur or is completely voltage independent. Third, determination of the fractional unblock by bbTBA at either low or high Ca^{2+} reveals deviations from a model in which open- and closed-state block is identical. The results support the view that bbTBA blockade of fully closed channels does not occur. We imagine two general types of explanation. First, a stronger voltage dependence of closed-channel block may minimize the contribution of closed-channel block at negative potentials. Second, voltage-dependent conformational changes among closed-channel states may permit block by bbTBA. The analysis supports the latter view, suggesting that bbTBA blockade of fully closed channels does not occur, but the ability of bbTBA to block a closed channel requires movement of one or more voltage sensors. Models in which block is coupled to voltage sensor movement can qualitatively account for (1) the ability of open-channel block to better fit block of conductance–voltage curves at high Ca^{2+}; (2) the voltage dependence of fractional availability; and (3) the fractional unblock at different open probabilities. BK channels appear to undergo voltage-dependent conformational changes among closed states that are permissive for bbTBA block.

The Journal of General Physiology

INTRODUCTION

Mechanistic studies of ion channel block have provided important insight into many fundamental aspects of ion channel structure and function (Armstrong, 1971; Armstrong and Hille, 1972). This has included examination of the state dependence of drug and blocker access to blocking sites (Liu et al., 1997), the definition of structural elements of channels involved in gated access to channel-blocking sites (del Camino and Yellen, 2001), the relationship of blocker molecules to the ion permeation pathway and blocker interactions with permeant ions (Heginbotham and Kutluay, 2004; Kutluay et al., 2005), and the molecular mechanisms of inactivation (Choi et al., 1991). In *Shaker* K^+ channels, charged cytosolic channel blockers typically only reach their blocking position when the channel is open. Furthermore, a blocker generally must exit its blocking position before the channel can close (Demo and Yellen, 1991). Thus, the blocking position is considered to be within an aqueous central cavity (Zhou et al., 2001) and, in the closed channel, a constriction at the cytosolic end of the S6 inner helix prevents access to that central cavity (del Camino and Yellen, 2001). This simple block behavior is thought to be shared by a variety of blocking molecules, including both small quaternary ammonium (QA) blockers (Armstrong, 1971) and bulkier peptide blockers derived from the physiologically relevant N-terminal inactivation domains of either α or β subunits (Ruppersberg et al., 1991; Murrell-Lagnado and Aldrich, 1993; Rettig et al., 1994). As an extension of this similarity in blocking action, QA blockers and inactivation domains also exhibit strict competition for pore-blocking sites, with QA blockers producing a slowing of the onset of inactivation consistent with simple competition (Choi et al., 1991). Structural studies coupled with a mutant cycle analysis of Kv β1.2 peptide interactions with the Kv1.4 channel have provided a compelling view that inactivation domains fit snugly within the central cavity of open Kv channels (Zhou et al., 2001), thereby preventing both ion permeation and the channel-closing conformational change.

Correspondence to Christopher J. Lingle: clingle@morpheus.wustl.edu

Abbreviations used in this paper: bbTBA, *N*-(4-[benzoyl]benzyl)-*N,N,N*-tributylammonium; BK, large-conductance Ca^{2+}-activated K^+; GV, conductance–voltage; NPo, number of channels times open probability; Po, open probability; QA, quaternary ammonium.

The Rockefeller University Press $30.00
J. Gen. Physiol. Vol. 134 No. 5 409–436
www.jgp.org/cgi/doi/10.1085/jgp.200910251

For large-conductance Ca^{2+}-activated K^+ (BK)-type channels, several aspects of block and inactivation have not been easy to explain within the context of a simple open-channel block mechanism: (1) QA blockers typically do not produce the slowing of channel deactivation that is predicted by simple block (Li and Aldrich, 2004); (2) BK channel block by *N*-(4-[benzoyl]benzyl)-*N,N,N*-tributylammonium (bbTBA) exhibits kinetic features consistent with blockade of both open and closed channels (Wilkens and Aldrich, 2006); (3) QA blockers do not show competitive inhibition of the onset of BK channel inactivation (Solaro et al., 1997; Xia et al., 1999); and (4) BK channel inactivation exhibits features of a two-step inactivation process (Lingle et al., 2001; Benzinger et al., 2006) and, in some cases, recovery from inactivation can occur without obvious channel reopening (Solaro et al., 1997). Some of these properties may be explained by the idea that some blocking species may be able to occupy a position in the BK central cavity, both when the channel is open and when it is closed (Wilkens and Aldrich, 2006). However, block of BK channels by a peptide derived from the ShakerB N terminus exhibits clear evidence of state-dependent block (Li and Aldrich, 2006), indicative that the BK channel does undergo a conformational change during gating that increases access of some peptide blockers to a blocking position. One suggestion regarding the underlying physical basis for the differences between block by the peptides and block by QA compounds is that, unlike for Kv channels, perhaps the entryway into the BK central cavity is not completely occluded in closed channels (Wilkens and Aldrich, 2006). Furthermore, perhaps like the open MthK bacterial channel (Jiang et al., 2002), the overall central cavity of the BK channel may be much broader than that found in Kv channels. The idea of a central cavity of larger dimension is also supported by an analysis of sugar effects on ion conductance in BK channels (Brelidze and Magleby, 2005).

An important implication of the idea that pore-blocking molecules may have access to the BK central cavity both in open and closed conformations is that this suggests that, in BK channels, there may be no cytosolic gate for small molecules. As such, the conformational change that allows gated access of *Shaker* peptides to the BK channel would not be the movement of a gate directly leading to the increase in ion permeation, but perhaps an additional expansion of an opening to an already accessible central cavity. Definition of the precise temporal sequence through which molecules may gain access to the central cavity is therefore important for elucidating the nature of conformational changes that precede channel opening and which steps are directly coupled to the initiation of ion permeation.

Some of the most intriguing evidence supporting the idea that small molecules may have access to the BK central cavity when the channel is closed concerns the effects of bbTBA, a bulky derivative of tetrabutylammonium (Wilkens and Aldrich, 2006). At 1 or 4 μM Ca^{2+}, blockade by bbTBA exhibits properties consistent with both open- and closed-channel block (Wilkens and Aldrich, 2006). Furthermore, at high [bbTBA], current waveforms exhibit kinetic components that can only be explained by block of both closed and open channels. An important question unaddressed by this earlier work is the extent to which block of open and closed states shares similar properties, including affinity and voltage dependence. Given the importance of establishing the validity of this model of block of BK channels, here we have extended this earlier work in several ways. We have undertaken tests to define properties of closed-channel block and to examine block over a range of fractional activation at both 4 and 300 μM Ca^{2+}. In addition, we have evaluated the results in terms of physically plausible allosteric models of BK gating (Cui et al., 1997; Horrigan and Aldrich, 2002), which include multiple closed and open states that are traversed during gating. Although the present results confirm some aspects of the earlier observations concerning bbTBA (Wilkens and Aldrich, 2006), the new observations argue that blockade by bbTBA does not occur in a fully state-independent fashion, a possibility raised by Wilkens and Aldrich. Rather, the effects of bbTBA are best explained by the idea that channels in a full resting state, i.e., closed channels with no active voltage sensors, are not sensitive to block by bbTBA. However, blockade of closed channels by bbTBA may occur as soon as at least one voltage sensor becomes active.

MATERIALS AND METHODS

Oocyte handling and expression construct

The handling of stage IV *Xenopus laevis* oocytes for cRNA injection and expression was as described previously (Xia et al., 1999, 2002). The coding region of mSlo1 (provided by L. Salkoff, Washington University, St. Louis, MO; GenBank accession number NM_010610) was subcloned into an oocyte expression vector pXMX using the 5′ NotI and 3′ SalI restrictions sites in a segment containing multiple cloning sites. The pXMX vector was designed to contain multiple factors that may promote expression or increase RNA stability. At the 5′ end of the multiple cloning site segment, vector pXMX contains a Sp6 promoter, 45 bp (residues −48 to −2 upstream of ATG) of *Xenopus laevis* major beta globin (XLMBG), and 162 bp (residues −169 to −7 upstream of ATG) of *Shaker* channel noncoding sequence. Following the 3′ end of the multiple cloning site, the vector contains 142 bp (residues −9 to 130 relative to stop codon TAA) of XLMBG noncoding downstream sequence and a 45-bp poly-A segment, followed by linearization enzyme sites. The pXMX vector has been routinely used by this laboratory for expression of both α and β subunits in oocytes for several years (Xia et al., 2002; Zeng et al., 2003; Zhang et al., 2006).

Electrophysiology

Currents were recorded in the inside-out configuration (Hamill et al., 1981) with an Axopatch 200 amplifier (MDS Analytical Technologies). The Clampex program from the pClamp package (MDS Analytical Technologies) was used to drive stimulus protocols

and digitize currents. Pipettes were typically 1–2 MΩ and were coated with Sylgard 184 (Dow Corning) and fire-polished. Gigaohm seals were formed in frog Ringer ([in mM] 115 NaCl, 2.5 KCl, 1.8 $CaCl_2$, and 10 HEPES, pH 7.4) and, after excision, moved into flowing test solutions. The standard solution bathing the extracellular membrane face (pipette solution) contained (in mM) 140 K-methanesulfonate (MES), 20 KOH, 10 HEPES, and 2 $MgCl_2$, pH 7.0 (titration with MES). The composition of solutions used to bathe the cytoplasmic face of patch membranes was (in mM) 140 K-MES, 20 KOH, and 10 HEPES, with pH adjusted to 7.0 with MES. Preparation of solutions of different Ca^{2+} concentration was as described previously (Wei et al., 1994; Zhang et al., 2001). Solutions were titrated with Ca-MES or methanesulfonic acid solutions to obtain desired Ca^{2+} concentrations, as defined with a Ca^{2+}-sensitive electrode calibrated with commercial Ca^{2+} solutions (WPI). Solutions were exchanged at the pipette tip by a fast perfusion stepper system (SF-77B; Warner Instruments). All experiments were at room temperature (~22–25°C). Salts for solution preparation were obtained from Sigma-Aldrich. bbTBA was obtained from Spectra Group Limited. Stock solutions of 1 mM bbTBA in different Ca^{2+} solutions were prepared and stored frozen at −20°C. bbTBA solutions for experiments were prepared by dilution of stock solutions immediately before experiments. Stock solutions were used within 1 month.

Data analysis

Analysis of current recordings was accomplished either with Clampfit (MDS Analytical Technologies) or with programs written in this laboratory. To define the voltage dependence of blocking equilibria, conductance–voltage (GV) curves were constructed from measurements of steady-state current. For families of GV curves obtained within a patch, conductances were normalized to estimates of maximal conductance obtained in the absence of blocker. For definition of the voltage of half-activation (V_h) and voltage dependence of current activation (q), GV curves were fit with the following Boltzmann function:

$$G(V) = \frac{G_{\max}}{1+\exp^{\frac{-qF(V-V_h)}{RT}}}. \quad (1)$$

At activation potentials of +160 mV and more positive, in our hands there are often slow reductions of BK current in control saline, regardless of the magnitude of the current in a patch. This appears to reflect a slowly developing block, but it is also rapidly reversible because tail currents do not show the same decrement in current with command step duration. An additional complication is that, in the presence of bbTBA (or other blockers), such slow reductions in current are generally not observed. We have not identified any procedure that consistently circumvents this problem. The inclusion of the crown ether Ba^{2+} chelator, (+)-18-crown-6-tetra-carboxylic acid (Neyton, 1996), did not reduce such slow macroscopic current relaxations. To minimize the possibility that estimates of conductance may be distorted by such slow block, we have limited estimates of conductance and block at 100 or 300 μM Ca^{2+} to voltages of +120 mV or more negative and to voltages of +160 mV or lower at 4 μM Ca^{2+}.

Open-channel block

The basic open-channel blocking mechanism (OB model) is defined in Scheme 1, with the predictions for steady-state Po defined in Eq. 2.

$$C \rightleftharpoons O \underset{}{\overset{[X]/K_{bo}}{\rightleftharpoons}} B$$

(SCHEME 1)

$$Po(V,[X]) = \frac{1}{1+\frac{C}{O}+\frac{B}{O}} \quad (2)$$

Eq. 2 yields the following well-known expression for the dependence of conductance on voltage and blocker:

$$G(V,[X]) = \frac{G_{\max}}{1+\exp^{\frac{-qF(V-V_h)}{RT}}+\frac{[X]}{K_{bo}\exp^{\frac{-zbFV}{RT}}}}, \quad (3)$$

where q is charge movement associated with the activation equilibrium, V_h is the voltage of half-activation, and K_{bo} is the 0-voltage dissociation constant of blocker, X, for the open state, with z_b reflecting the intrinsic voltage dependence of the binding equilibrium. Because BK channel activation can be defined by distinct terms reflecting both Ca^{2+} and voltage-dependent allosteric equilibria (Horrigan et al., 1999; Cui and Aldrich, 2000), here we use general equations that, by incorporating both activation and block, allow a more direct assessment of predictions regarding the overall fractional block of conductance as a function of steady-state channel open probability (Po) at different Ca^{2+}. We have therefore approximated L in terms of the Horrigan-Cui-Aldrich formulation (Horrigan et al., 1999; Cui and Aldrich, 2000), in which activation of channel conductance by both voltage and Ca^{2+} is given by:

$$Po(V,A) = \frac{1}{1+(\frac{1}{L(V)})(\frac{1+J}{1+JD})^4(\frac{1+[Ca^{2+}]/K_c}{1+C[Ca^{2+}]/K_c})^4}, \quad (4)$$

where $L(V) = L0\exp^{z_L FV/RT}$, $J = J0\exp^{z_J FV/RT}$, with L defining the C-O equilibrium constant, z_L, its voltage dependence, $J0$ is the voltage sensor equilibrium constant at 0 mV, with z_J defining the voltage dependence of J, D is the coupling constant between L and J, K_c is the binding constant of agonist [A] to the closed conformation, and C is the coupling constant between the ligand binding equilibrium and L. This formulation ignores the weak coupling (E) that occurs between the Ca^{2+}-binding equilibrium and the voltage sensor equilibrium (Horrigan and Aldrich, 2002).

For many experiments, we examine blockade at a single Ca^{2+} concentration. When fitting data obtained in the presence of blocker, it is desirable that parameters describing activation be constrained to those obtained in the absence of blocker. Therefore, Eq. 4 can be simplified to reflect the Po at a single Ca^{2+} concentration:

$$Po(V) = \frac{1}{1+(\frac{1}{L'(V)})(\frac{1+J'}{1+J'D'})^4}, \quad (5)$$

where

$$L' = L(V)(\frac{1+C[Ca^{2+}]/K_c}{1+[Ca^{2+}]/K_c})^4.$$

Here, J′ and D′ differ from J and D as defined over all Ca^{2+} and voltage because of the small effect of coupling between the ligand binding and the voltage sensor equilibrium. Eq. 5 provides an empirical description of the activation behavior for Slo1 at a given [Ca^{2+}]. For all cases in which either single or multiple GV curves in the absence of blocker were fit to define activation parameters, z_L and z_J were constrained to 0.3 e and 0.58 e, respectively, whereas

equilibrium and coupling constants were allowed to vary. Once the optimal fit to the activation GV curves was obtained, all activation constants were then fixed during fitting of the GV curves in the presence of blocker.

Using terms for activation, Eq. 3 can then be recast as:

$$Po(V,[X]) = \frac{1}{1+\frac{1}{L'}\left(\frac{1+J'}{1+J'D'}\right)^4 + \frac{[X]}{K_{bo}\exp^{\frac{-z_bFV}{RT}}}}. \quad (6)$$

For simplicity in the equations below, we also define the following:

$$1/\bar{L} = \frac{1}{L'}\left(\frac{1+J'}{1+J'D'}\right)^4.$$

Eq. 6 can be derived directly from the following open-channel block model (Scheme 1a) for activation and block over a range of voltages at a single agonist concentration.

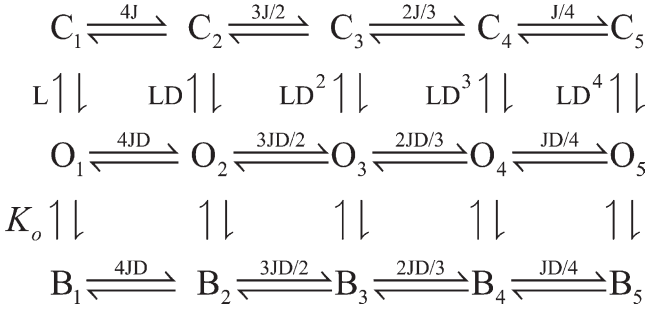

(SCHEME 1a)

Block of both open and closed states

We also evaluate whether a blocker may act by binding to the same site in both open and closed states, as given in Scheme 2 (CB-OB model).

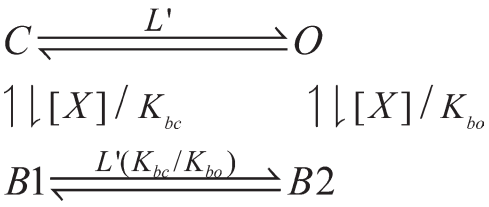

(SCHEME 2)

For Scheme 2, the predictions for Po as a function of voltage and blocker concentration [X] are:

$$Po(V,[X]) = \frac{1}{1+\frac{1}{\bar{L}}+\frac{1}{\bar{L}}\frac{[X]}{K_{bc}\exp^{\frac{-z_bFV}{RT}}} + \frac{[X]}{K_{bo}\exp^{\frac{-z_bFV}{RT}}}}, \quad (7)$$

where K_{bc} and K_{bo} reflect the dissociation constants for binding to either closed or open channels, respectively, and z_b is the valence of the blocking equilibrium, assuming block of both open and closed states has an identical voltage dependence. Defining $W = K_{bc}/K_{bo}$, an allosteric constant coupling the drug-binding equilibria to L′, Eq. 7 becomes:

$$Po(V,[X]) = \frac{1}{1+\frac{1}{\bar{L}}+\frac{1}{\bar{L}}\frac{[X]}{W*K_{bo}\exp^{\frac{-z_bFV}{RT}}} + \frac{[X]}{K_{bo}\exp^{\frac{-z_bFV}{RT}}}}. \quad (8)$$

When W = 1, Eq. 8 describes a completely state-independent block scheme. When W >> 1, i.e., when closed-channel block is minimal, Eq. 8 becomes identical to Eq 6. When $K_{bc} << K_{bo}$ (i.e., W << 1), Eq. 8 describes a strict closed-channel block mechanism.

For situations in which open- and closed-channel block exhibits different voltage dependencies,

$$W(V) = \frac{K_{bc}}{K_{bo}}\exp^{\frac{-(z_c-z_o)FV}{RT}}.$$

This adds an additional free parameter to Eq. 8, which imparts a voltage-dependent effect on the gating equilibrium:

$$Po(V,[X]) = \frac{1}{1+\frac{1}{\bar{L}}+\frac{1}{\bar{L}}\frac{[X]}{K_{bc}\exp^{\frac{-z_cFV}{RT}}} + \frac{[X]}{K_{bo}\exp^{\frac{-z_oFV}{RT}}}}. \quad (9)$$

Eqs. 8 and 9 can be derived directly from a 20-state blocking scheme (e.g., General Scheme 2) for activation at a single [Ca^{2+}], but including blockade of both open and closed states.

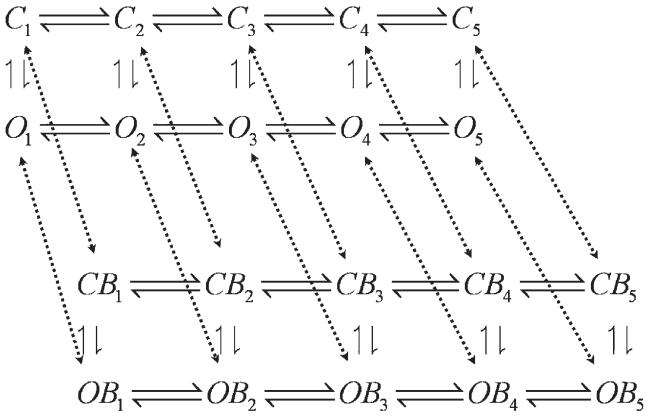

(GENERAL SCHEME 2)

We designate the completely state-independent block scheme in which $K_{bc} = K_{bo}$ and $z_o = z_c$ as Scheme 2a (also see Fig. S2). We designate the specific case in which closed-channel block is voltage independent ($z_c = 0$) and $K_{bc}(0) = K_{bo}(0)$ as Scheme 2b, the case in which $K_{bc}(0) \neq K_{bo}(0)$ and $z_c = 0$ as Scheme 2b′, and the case that $K_{bc} \neq K_{bo}$ and $z_o \neq z_c$ as Scheme 2′.

Access to a blocking site depends on movement of voltage sensors

We have also evaluated models in which we postulate that conformational events occur in closed channels in conjunction with voltage sensor movement that then permit access of blockers to blocking sites.

In Scheme 3 (also see Fig. S3), access of blocker to a blocking site does not occur until at least one voltage sensor has been activated.

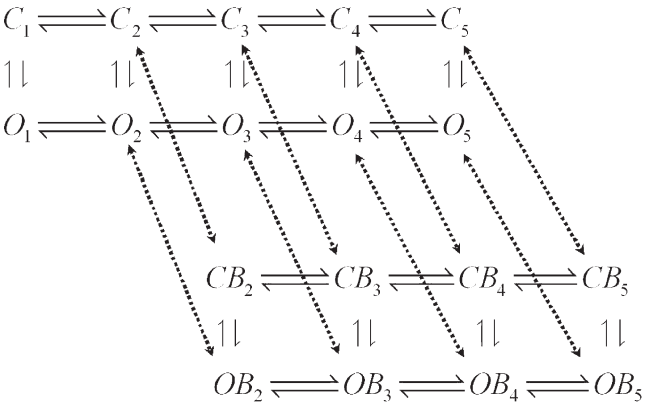

(GENERAL SCHEME 3)

An alternative version of this scheme would allow blockade of state O_1, but not state C_1. However, under all conditions evaluated here, occupancy of state O_1 is sufficiently negligible that such a model is largely indistinguishable from Scheme 3. For Scheme 3, some of the symmetry of the full allosteric models is lost, yielding a somewhat more complicated steady-state current prediction. For the general case in which $K_{bc} \neq K_{bo}$ and $z_c \neq z_o$, the following general expression can be derived:

$$Po(V,[X]) = \frac{1}{1+\frac{1}{L'}\frac{(1+J')^4}{(1+J'D')^4}+Cblck+Oblck}, \quad (10)$$

where

$$Cblck = \frac{(1+J')^4-1}{L'(1+J'D')^4}\frac{[X]}{K_{bc}\exp^{\frac{-z_cFV}{RT}}}$$

and

$$Oblck = \frac{(1+J'D')^4-1}{(1+J'D')^4}\frac{[X]}{K_{bo}\exp^{\frac{-z_oFV}{RT}}}$$

We term the specific case that $K_{bc} = K_{bo}$ and $z_c = z_o$ as Scheme 3a, the case in which $K_{bc} = K_{bo}$ and $z_c = 0$ as Scheme 3b, the case that $K_{bc} \neq K_{bo}$ and $z_c = 0$ as Scheme 3b′, and the case in which $K_{bc} \neq K_{bo}$ and $z_c \neq z_o$ as Scheme 3′.

Affinity for the blocking site increases with number of active voltage sensors

We also consider a case in which voltage sensor movement is required for block to occur, but that blocking affinity scales with the number of active voltage sensors (Scheme 4 and Fig. S4). For activation at a single [Ca^{2+}], this yields the following expression for steady-state Po:

$$Po(V,[X]) = \frac{1}{1+\frac{1}{L'}\frac{(1+J')^4}{(1+J'D')^4}+Cblck+Oblck}, \quad (11)$$

where

$$Cblck = \frac{4J'(1+J')^3}{L'(1+J'D')^4}\frac{[X]}{K_{bc}\exp^{\frac{-z_cFV}{RT}}}$$

and

$$Oblck = \frac{4J'D'(1+J'D')^3}{(1+J'D')^4}\frac{[X]}{K_{bo}\exp^{\frac{-z_oFV}{RT}}}$$

The specific case in which $K_{bc} = K_{bo}$ and $z_c = z_o$ is termed Scheme 4a, the case in which $K_{bc} = K_{bo}$ and $z_c = 0$ is referred to as Scheme 4b, and the case in which $K_{bc} \neq K_{bo}$ and $z_c = 0$ is referred to as Scheme 4b′. For simplicity, we omit consideration of Scheme 4 from most sections of this paper.

Equations for block in conjunction with a full allosteric activation model

For some datasets, we also used equations based on a full allosteric activation model for BK gating (Horrigan and Aldrich, 2002), thereby allowing simultaneous fitting of GV curves obtained at multiple Ca^{2+} and multiple bbTBA. For open-channel block (Scheme 1), the blocking equilibrium is defined by:

$$Po(Ca,V,[X]) = \frac{1}{1+\frac{1}{L}\frac{(1+J+K+JKE)^4}{(1+JD+KC+JDKCE)^4}+\frac{[X]}{K_{bo}\exp^{\frac{-z_oFV}{RT}}}}, \quad (12)$$

where J, K, and L represent the voltage sensor, Ca^{2+} binding, and C-O equilibria, and D, C, and E represent coupling constants (Horrigan and Aldrich, 2002). Similarly, the equilibrium predictions for a model in which both open and closed channels can be blocked (Scheme 2) is the following:

$$Po(Ca,V,[X]) = \frac{1}{1+\frac{1}{L}\frac{Cterm}{Oterm}+\frac{[X]}{K_{bo}\exp^{\frac{-z_oFV}{RT}}}+\frac{1}{L}\frac{Cterm}{Oterm}\frac{[X]}{K_{bc}\exp^{\frac{-z_cFV}{RT}}}}, \quad (13)$$

where $C_{term} = (1+J+K+JKE)^4$ and $O_{term} = (1+JD+KC+JDKCE)^4$.

Similarly, Scheme 3, in which voltage sensor movement is required for block to occur, can be described by:

$$Po(Ca,V,[X]) = \frac{1}{1+\frac{1}{L}\frac{Cterm}{Oterm}+Cblck+Oblck}, \quad (14)$$

where

$$Cblck = \frac{1}{L}\frac{Cterm-(1+K)^4}{Oterm}\frac{[X]}{K_{bc}\exp^{\frac{-z_cFV}{RT}}}$$

and

$$Oblck = \frac{Cterm-(1+K)^4}{Oterm}\frac{[X]}{K_{bo}\exp^{\frac{-z_oFV}{RT}}}$$

This equation reflects that Ca^{2+}-binding steps among states with 0 active voltage sensors are removed from the set of all blocked-closed states and the set of all blocked-open states.

Derivation of a similar equation for the case in which the blocking equilibria scales linearly with the number of active voltage sensors (Scheme 4) is less straightforward because in the full allosteric model, the scaled blocking rates result in allosteric effects on gating equilibrium steps that involve subunit-specific coupling between voltage sensors and Ca^{2+} sensors (Horrigan and Aldrich, 2002).

However, if we assume that this coupling is minor, i.e., that E = 1, one can derive the following equation:

$$Po(Ca,V,[X]) = \frac{1}{1+\frac{1}{L}\frac{(1+J+K+JK)^4}{(1+JD+KC+JDKC)^4}+Cblck+Oblck}, \quad (15)$$

where

$$Cblck = \frac{4J(1+J)^3(1+K)^4}{L(1+JD+KC+JDKC)^4}\frac{[X]}{K_{bc}\exp^{\frac{-z_cFV}{RT}}}$$

and

$$Oblck = \frac{4JD(1+JD)^3(1+KC)^4}{(1+JD+KC+JDKC)^4}\frac{[X]}{K_{bo}\exp^{\frac{-z_oFV}{RT}}}$$

When comparing Scheme 4 to other models, all fitting was done with the assumption of E = 1.

Two distinct blocking sites

We also considered a blocking model involving two distinct binding sites for bbTBA, where one site is accessible in both open and closed channels (states B_1 and B_2), and one site (B_c) is only reached when channels are open. Because this model did not better explain the results than the single-site models, we only briefly mention this model in the Results. The specific two-site model we considered is summarized in Scheme 5:

$$\begin{array}{ccccc} C & \underset{}{\overset{L'}{\rightleftharpoons}} & O & \underset{}{\overset{[X]/K_{2o}}{\rightleftharpoons}} & B_c \\ \uparrow\downarrow [X]/K_{1c} & & \uparrow\downarrow [X]/K_{1o} & & \uparrow\downarrow [X]/K_{1o2} \\ B_1 & \underset{}{\overset{L'(K_{1c}/K_{1o})}{\rightleftharpoons}} & B_2 & \underset{}{\overset{(K_{1o}/K_{1o2})[X]/K_{2o}}{\rightleftharpoons}} & B_{2c} \end{array}$$

(SCHEME 5)

We define two allosteric coupling constants: $W = K_{1c}/K_{1o}$ and $Y = K_{1o}/K_{1o2}$. From Scheme 4, the dependence of Po on voltage, [bbTBA], and Ca^{2+} is:

$$Po(Ca,V,[X]) = \frac{1}{1+\frac{1}{L}\frac{Cterm}{Oterm}+Trm1+Trm2+Trm3}, \quad (16)$$

where

$$Trm1 = \frac{1}{L}\frac{Cterm}{Oterm}\frac{[X]}{W * K_{1o}\exp^{\frac{-z_{1c}FV}{RT}}},$$

$$Trm2 = \frac{[X]}{K_{1o}\exp^{\frac{-z_{1o}FV}{RT}}}+\frac{[X]}{K_{2o}\exp^{\frac{-z_{2o}FV}{RT}}},$$

and

$$Trm3 = \frac{Y[X][X]}{K_{2o}K_{1o}\exp^{\frac{-z_{2o}FV}{RT}}\exp^{\frac{-z_{1o}FV}{RT}}}$$

When W = 1, binding to site 1 is identical both in open and closed channels. When Y = 1, binding to either site does not influence binding to the other site. In practice, the number of free parameters in this function can limit its utility. However, we explored this model with the simplifying assumptions that the sites are independent (Y = 1) and that W = 1. In addition, we assumed that binding to site 1 is voltage independent.

Kinetic simulations

Simulations of the kinetic behavior of different blocking models was done with a modified version of the IChSim program (see Online supplemental material below) for single-channel and macroscopic current simulations developed by J.A. De Santiago-Castillo (Jefferson University, Philadelphia, PA). All simulations used a population of 100 channels with an open-state conductance of 200 pS. Using simulated currents activated with various kinds of standard stimulation protocols, predicted GVs, fractional unblock curves, fractional availability curves, and tail currents were generated for each model. MathCad 8.0 (PTC Corporation) was also used to generate predicted GV curves, fractional unblock curves, and fractional availability curves to confirm results from the kinetic simulations. In all cases, steady-state predictions derived from analysis of simulated currents generated by IchSim agreed with the predictions based on steady-state equations implemented in MathCad.

Online supplemental material

Figs. S1–S4 summarize details of blocking Schemes 1–4, respectively. Fig. S5 shows that voltage dependence of closed-channel block, by altering the effective gating charge in the CB–OB transition, predicts unusual current activation and deactivation behavior. Fig. S6 highlights the inability of particular forms of Scheme 2 to produce triphasic current relaxations. Fig. S7 expands on Fig. 12 and examines the predictions of various closed-channel blocking schemes for the behavior of fractional availability in the presence of blocker species. Fig. S8 expands on Fig. 13 and shows that deactivation behavior is not particularly useful for distinguishing among different closed-channel blocking schemes. The modified version of the IChSim program used for kinetic simulations is also included in the supplemental material. The supplemental material is available at http://www.jgp.org/cgi/content/full/jgp.200910251/DC1.

RESULTS

In this paper, we show that, although bbTBA does block both open and closed channels, bbTBA does not block in a fully state-independent fashion. The results support the view that, independent of specific blocking model, closed channels with inactive voltage sensors are insensitive to block by bbTBA. Such a result might arise either because (1) a strong closed-state voltage dependence minimizes bbTBA block at negative potentials, or (2) there are voltage-dependent conformational changes among closed states permissive for block. Our analysis tends to exclude the possibility of strong closed-state voltage dependence, while supporting the view that block is coupled to conformational changes among closed states. However, the results provide no direct insight into the physical basis for the inability of bbTBA to block closed channels with inactive voltage sensors. We envision two primary mechanistic explanations for the dependence of closed-channel block

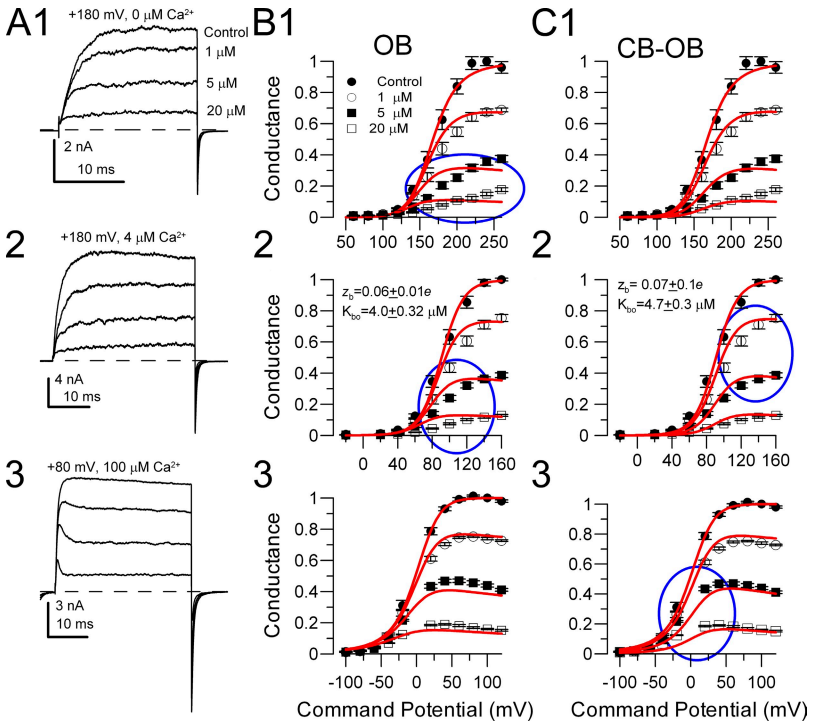

Figure 1. Steady-state block of BK currents by bbTBA. (A) BK currents were activated by steps to +180 mV with 0 Ca^{2+} (1), 4 μM Ca^{2+} (2), or 100 μM Ca^{2+} (3), along with 0, 1, 5, or 20 μM bbTBA. (B) GV curves generated from steady-state current levels were determined for each Ca^{2+} concentration (1, 0 μM; 2, 4 μM; 3, 100 μM) in the presence of various concentrations of bbTBA, and all curves were fit simultaneously with a strict open-channel blocking model (Eq. 12). Details of fitting are given in Materials and methods and Results. The optimal fit (red lines) for the open-channel block (OB) assumption yielded K_{bo} = 4.0 ± 0.32 μM with z_b = 0.06 ± 0.01 *e*. (C) The same GV curves displayed in B were simultaneously fit to Eq. 13 with the constraint that $K_{bo} = K_{bc}$ and $z_o = z_c$. In this case, $K_{bo} = K_{bc}$ = 4.7 ± 0.3 μM with z_b = 0.07 ± 0.1 *e*. Blue ovals highlight regions of the curves in which the fitted curves deviate markedly from the observed results, with the OB model doing poorly at low Ca^{2+}, and the CB–OB model being inadequate at higher Ca^{2+}.

on closed-state conformation changes: (1) a change in bbTBA access to the central cavity perhaps involving an expansion of an aperture separating the central cavity from the bulk cytosol, and (2) a change in bbTBA binding affinity within the central cavity. Although this issue is unanswered in this paper, these potential explanations of physical mechanism may help guide understanding of the results and analysis.

The apparent state dependence of block by bbTBA differs between low and high Ca^{2+}

Slo1 currents were activated in inside-out patches at various voltage steps with 0, 4, or 100 μM cytosolic Ca^{2+}. At each [Ca^{2+}], currents were generated in the presence and absence of 0, 1, 5, and 20 μM bbTBA in the solution bathing the cytosolic face of the membrane (Fig. 1). At higher [Ca^{2+}] in which current activation is faster, the slower block by bbTBA produces a time-dependent reduction in outward current (traces at 100 μM Ca^{2+}). Typically, any individual patch was only used to generate GV curves at one [Ca^{2+}], but over the full range of [bbTBA]. Because rapid unblock occurred during tail currents, measurements of steady-state current levels at different voltages were used for the generation of GV curves at each [Ca^{2+}] (Fig. 1, B and C). Note that identical GV curve values are plotted in B and C, but each panel was fit with a different blocking model. Qualitatively, the features of block, particularly with 20 μM bbTBA, exhibit differences at lower and higher Ca^{2+}. In particular, at low open probabilities, bbTBA produces more appreciable block at lower Ca^{2+} concentrations than it does at higher Ca^{2+} concentrations.

To assess the ability of different channel block models to describe bbTBA behavior, we fit each family of GV curves over all bbTBA concentrations both with the strict open-channel block model (OB model; Scheme 1a) and with a model in which both open and closed channels are blocked identically (CB-OB model; Scheme 2a). The GV curves at each [Ca^{2+}] were fit with Eq. 12 (Fig. 1 B) to assess the adequacy of the OB model, and then fit with Eq. 13 (Fig. 1 C) to assess the CB-OB model. Block parameters are given in Fig. 1 and its legend. Neither scheme does a good job of fitting the GV curves over all Ca^{2+}. As highlighted by the blue ovals (Fig. 1 B, 1 and 2), at 0 and 4 μM Ca^{2+}, the OB model failed to describe the extent of block produced by the higher concentrations of bbTBA, particularly at lower fractional conductances. In contrast, at 100 μM Ca^{2+}, the CB-OB model overestimated the extent of block observed with higher bbTBA at lower fractional conductances (Fig. 1 C, 3). Furthermore, the best fit of the CB-OB model does not describe the upward trend in conductance at the most positive voltages with bbTBA (e.g., Fig. 1 C, 2).

We also fit each of the GV curves individually with Eq. 8, with W constrained to either 100,000 (the OB assumption) or 1 (the CB-OB assumption). Fitting of the GV curves at a single Ca^{2+} resulted in better approximations of the data. However, consistent with Fig. 1, at 0 and 4 μM, the CB-OB model did a much better job of reproducing the specific curvature of the data. Similarly, at 100 (or 300 μM) Ca^{2+}, the OB model better describes the GV curves. This was also supported by a comparison of the sum of the squares of the fit obtained with each model. Another factor supporting this idea is

that the parameters of the best fit for either the OB or CB-OB model differ among low and high [Ca^{2+}]. In particular, the voltage dependence of block switches from block being favored by more positive potentials at higher Ca^{2+} to being weakened at higher voltages with low Ca^{2+}. Similarly, the estimated K_b values are not consistent across Ca^{2+} concentrations. The inability of either model to yield a generally consistent set of parameters for the blocking reaction can only indicate that neither model is an appropriate description of block of BK channels by bbTBA. The dependence of block on [Ca^{2+}] suggests that block by bbTBA may not be entirely state independent.

Physically plausible models for activation and block

The above results suggest that not all open or closed states are equivalent in their sensitivities to bbTBA. Here, we ask whether there is a blocking scheme that may better account for the apparently differential blocking effects of bbTBA at low and high Ca^{2+}. We base our examination of the predictions for bbTBA block on physically plausible gating models of BK channel activation (Cui and Aldrich, 2000; Horrigan and Aldrich, 2002). To examine predictions for blockade at a single [Ca^{2+}], blocking models were constructed based on a basic 10-state activation model (see Scheme 1a and Fig. S1 A), in which activation of BK channels at a given [Ca^{2+}] involves movement of four voltage sensors defined by equilibrium constant (J′(0)) and a closed-open conformational equilibrium (L′(0)) (Horrigan and Aldrich, 2002). Channel activation is coupled to voltage sensor activation via coupling constant, D′. The "prime" designations are used to highlight that these values are effectively altered by the fact that a complete gating model would also include tiers accounting for Ca^{2+}-dependent activation, such that the values J′, L′, and D′ are not identical to the constants used in the full allosteric gating scheme. Predictions of different models of block were examined using two nominal Ca^{2+} concentrations, 4 and 300 µM (see Materials and methods and Figs. S1–S4 for additional detail of different blocking models). Values chosen for rates of voltage sensor movement and channel gating rates (Table I) were guided by previous estimates from Horrigan and Aldrich (2002) and adjusted to yield an overall V_h that generally approximates experimental observations obtained at 4 and 300 µM Ca^{2+}, with channel activation and deactivation rates generally consistent with observed data.

We evaluated three main categories of blocking mechanism: (1) only open channels are blocked (Scheme 1); (2) both open and closed states are blocked (Scheme 2); and (3) both open and closed channels are blocked, but at least one voltage sensor must be activated in order for block to occur (Scheme 3). We also considered one variation of Scheme 3, in which block depends on voltage sensor movement, but the forward rate of block scales with the number of active voltage sensors (Scheme 4). One earlier observation that justifies consideration of the idea that voltage sensor movement may result in steps permissive for block is that closed-state inactivation of BK channels depends on voltage-dependent steps that occur in the absence of channel opening (Ding and Lingle, 2002). For Schemes 2–4, we considered several specific cases. First, for Schemes 2a, 3a, and 4a, we assumed that the open- and closed-channel blocking equilibria were identical as were their voltage

TABLE I

Rates for current simulations using 10-state activation model

4 µM Ca^{2+}	C1–C2	C2–C3	C3–C4	C4–C5	z_J	z_L
$\alpha(0)_c$	4,480	3,360	2,240	1,120	0.29 *e*	
$\beta(0)_c$	30,000	60,000	90,000	120,000	−0.29 *e*	
	C1–O1	C2–O2	C3–O3	C4–O4	C5–O5	
$\delta(0)$	0.4	7.344	120	288	350	0.212 *e*
$\gamma(0)$	3,200	2,350.08	1,536	147.456	7.168	−0.088 *e*
	O1–O2	O2–O3	O3–O4	O4–O5	*z*	
$\alpha(0)_o$	22,400	16,800	11,200	5,600	0.29 *e*	
$\beta(0)_o$	6,000	12,000	18,000	24,000	−0.29 *e*	
300 µM Ca^{2+}	C1–C2	C2–C3	C3–C4	C4–C5	z_J	
$\alpha(0)_c$	6,400	4,800	3,200	1,600	0.29 *e*	
$\beta(0)_c$	12,000	24,000	36,000	48,000	−0.29 *e*	
	C1–O1	C2–O2	C3–O3	C4–O4	C5–O5	
$\delta(0)$	24	340	6,000	6,000	6,000	0.212 *e*
$\gamma(0)$	2,227	841.31111	395.9111	10.5576	0.2815368	−0.088 *e*
	O1–O2	O2–O3	O3–O4	O4–O5	*z*	
$\alpha(0)_o$	40,000	30,000	20,000	10,000	0.29 *e*	
$\beta(0)_o$	2,000	4,000	6,000	8,000	−0.29 *e*	

Numbers are rates (s^{-1}) for the indicated transitions (e.g., C_1–C_2, state C1 to state C2). Calculated allosteric constants based on microscopic rates: L′ (4 µM) = 0.000125; D′ (4 µM) = 25; J′ (4 µM) = 0.037333; L′ (300 µM) = 0.0107768; D′ (300 µM) = 37.5; J′ (300 µM) = 0.1333333; z_L = 0.3 *e*; z_J = 0.58 *e*.

dependencies. In Schemes 2b, 3b, and 4b, we assumed that closed-state block was voltage independent, but $K_{bc} = K_{bo}$. Finally, for all schemes, we also examined variations in which both the binding affinities and voltage dependencies of open- and closed-channel block varied independently (termed 2′, 3′, and 4′). Because Scheme 4 was not clearly superior to Scheme 3 in accounting for the key aspects of block by bbTBA, to simplify this presentation we minimize further consideration of Scheme 4. Rates of block for simulations were chosen to approximate the macroscopic behavior of bbTBA (Table II).

Simulations with models in which block is dependent on voltage sensor movement reproduce differential effects of bbTBA on GV curves at low and high Ca^{2+}

Examples of simulated currents based on various blocking schemes (Schemes 1a, 2a, and 3a) are shown in Fig. 2 for a blocker concentration that is approximately sixfold the K_b for block of the open channel at 0 mV. For all models, this produces an ~90% block at a potential of +200 mV. Resulting GV curves were determined at different effective blocker concentrations, both for 4 μM Ca^{2+} (Fig. 3, left-hand panels) and for 300 μM Ca^{2+} (Fig. 3, middle panels). In each case, the families of GV curves were fit with Eq. 8, either with W = 1 (red lines; full OB-CB model equivalent to the predictions of Scheme 2a) or W = 100,000 (blue lines; full OB model equivalent to the predictions of Scheme 1a). For the GV curves explicitly generated by Scheme 2a, Eq. 8 with W = 1 yielded an essentially perfect fit, whereas similarly for the GV curves generated by Scheme 1a, Eq. 8 with W = 100,000 yielded an essentially perfect fit. However, for GV curves generated by alternative blocking models, it can be seen that the families of GV curves exhibit interesting differences in their ability to be fit under the constraints of Eq. 8. We used two types of comparisons to assess the ability of either the strictly state-independent model or open-channel block model to fit the GV curves. First, we simply determined the total sum of squares error for different fits (not depicted). Second, we determined the absolute error of a given fit for the full set of GV curves at each voltage (Fig. 3, right-hand panels). The former provides a direct measure of whether a given set of GV curves is better fit by one or the other model, whereas the latter provides a visual picture of the range of voltages over which deviations of a particular model are most pronounced.

The primary conclusion here is that, when currents are simulated by a scheme in which blockade depends on movement of voltage sensors (Scheme 3a), the CB-OB

TABLE II

Parameters for block and allosterically coupled changes in activation used in simulations

	Complete state-independent block		
Scheme 2a			
Block parameters (rates in s^{-1})		Allosterically altered parameters	
$f_c(0)$	0–5,000 (z = 0.05 *e*)		
$b_c(0)$	350 (z = −0.05 *e*)		
$f_o(0)$	0–5,000 (z = 0.05 *e*)		
$b_o(0)$	350 (z = −0.05 *e*)		
Scheme 2b	Closed channel block is voltage independent. To maintain microscopic reversibility, voltage dependence of CB–OB transitions is allosterically influenced.		
$f_c(0)$	0–5,000 (z = 0.0 *e*)	z (δ(0))	0.262 *e*
$b_c(0)$	350 (z = −0.0 *e*)	z (γ(0))	−0.138 *e*
$f_o(0)$	0–5,000 (z = 0.05 *e*)		
$b_o(0)$	350 (z = −0.05 *e*)		
Scheme 3a	Block dependent on movement of at least one voltage sensor		
$f_c(0)$	0–5,000 (z = 0.05 *e*)		
$b_c(0)$	350 (z = −0.05 *e*)		
$f_o(0)$	0–5,000 (z = 0.05 *e*)		
$b_o(0)$	350 (z = −0.05 *e*)		
Scheme 3b	Block dependent on movement of at least one voltage sensor, but closed-channel block is voltage independent. To maintain microscopic reversibility, voltage dependence of CB–OB transitions is allosterically influenced.		
$f_c(0)$	0–5,000 (z = 0.0 *e*)	$z (\delta(0))_o$	0.262 *e*
$b_c(0)$	350 (z = −0.0 *e*)	$z (\gamma(0))_o$	−0.138 *e*
$f_o(0)$	0–5,000 (z = 0.05 *e*)		
$b_o(0)$	350 (z = −0.05 *e*)		
Scheme 1a	Open-channel block		
$f_{on}(0)$	0–5,000 (z = 0.05 *e*)		
$b_o(0)$	350 (z = −0.05 *e*)		

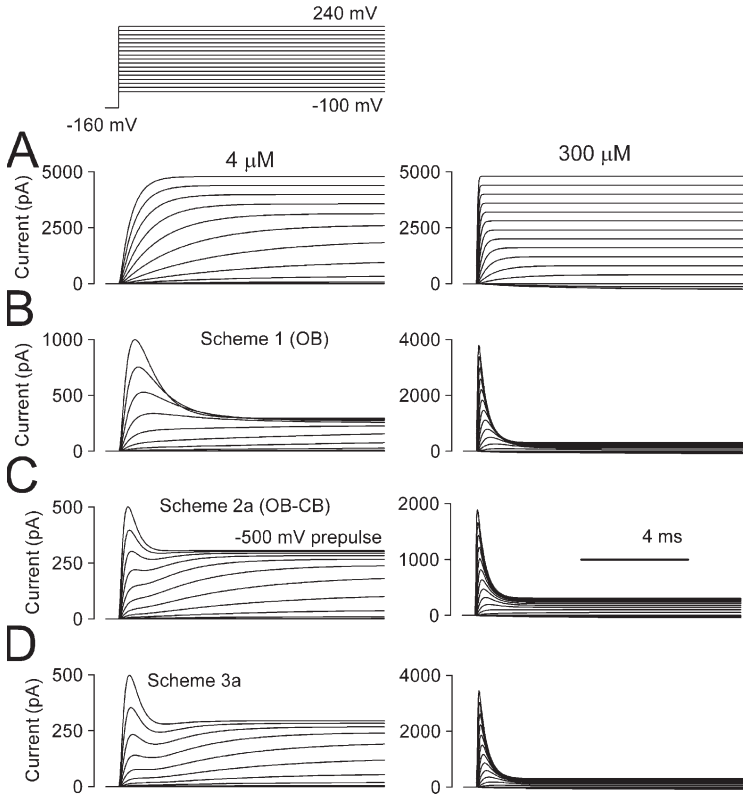

Figure 2. Current simulations with different blocking models. (A) Families of traces show control currents (no bbTBA) simulated with the indicated voltage protocol and either 4 μM Ca^{2+} (left) or 300 μM Ca^{2+} (right) using the 10-state activation model (Fig. S1 A). (B) Currents were simulated with classical open-state block in conjunction with the 10-state activation model (Scheme 1a). The slower onset of block in comparison to models with block of closed states reflects the coupling of inactivation to activation. (C) Traces show currents activated by the same conditions but with blockade defined by the full state–independent blocking model (Scheme 2a) with $K_{bo} = K_{bo}$ and $z_o = z_c$. Note the prominent triphasic currents at 4 μM Ca^{2+}. (D) Traces show currents simulated with Scheme 3a (block depends on activation of at least one voltage sensor) as well as prominent triphasic current relaxations at 4 μM.

equation (Eq. 8; W = 1) provides a better fit to the 4-μM GV curves, whereas the OB equation (Eq. 8; W = 100,000) provides the better fit to the 300-μM GV curves. This qualitatively approximates the situation observed for the bbTBA block of BK currents shown in Fig. 1 and suggests that neither a fully state-independent CB-OB model nor a strict OB model adequately describes bbTBA block.

As shown below, the basic OB model (Scheme 1a) clearly results in behaviors that are distinct from our observations, as also noted previously (Wilkens and Aldrich, 2006). For similar reasons, another scheme, not mentioned above, in which only channels with four activated voltage sensors are blocked, can also be excluded. We also found that a trapping model in which closed channels cannot be blocked, but open-blocked channels can close (Lingle, 1983; Neely and Lingle, 1986; Wilkens and Aldrich, 2006), makes predictions inconsistent with observations. We also tested a two-site model (see Materials and methods) in which block is posited to occur at two sites: an open-channel block site, and a peripheral site that is accessible in both open and closed states. This model potentially involves a large number of parameters, although various simplifying assumptions can be made to reduce model complexity. However, two aspects of this model led us to exclude it from consideration: first, the open-channel block portion of the model predicts properties of tail currents inconsistent with observation and, second, the best fits of this model tend to converge to values similar to the single-site models, with the open-channel block site having very low affinity. We will not consider these latter models in more detail.

Models in which block is coupled to voltage sensor movement better fit GV curves at both low and high Ca^{2+}

In Fig. 1, data for the GV curves at each Ca^{2+} were obtained in separate sets of patches. To better constrain blocking parameters, it would be desirable to fit GV curves obtained at both low and high Ca^{2+} simultaneously. Data were therefore collected from a set of patches in which the effects of 0, 1, 5, and 20 μM bbTBA were tested at both 4 and 300 μM (Fig. 4). With activation parameters defined from fitting GV curves with 0 bbTBA, the full family of GV curves were then fit simultaneously with equations for Scheme 2a (Eq. 13, complete state-independent block), Scheme 1a (Eq. 12, strictly open-channel block), and Scheme 3a (Eq. 14, block dependent on initial voltage sensor movement), in all cases with the assumption that block of open and closed states has an identical affinity ($K_{bc} = K_{bo}$) and voltage dependence ($z_o = z_c$). It can be clearly seen that both Scheme 2a (Fig. 4 A) and Scheme 1a (Fig. 4 B) fail to describe important features of the GV curves, consistent with the simulations of Fig. 3. In contrast, Scheme 3a, in which block depends on movement of at least one voltage sensor, captures the shape of the GV curves particularly at low Po for both 4 and 300 μM Ca^{2+} (Fig. 4 C).

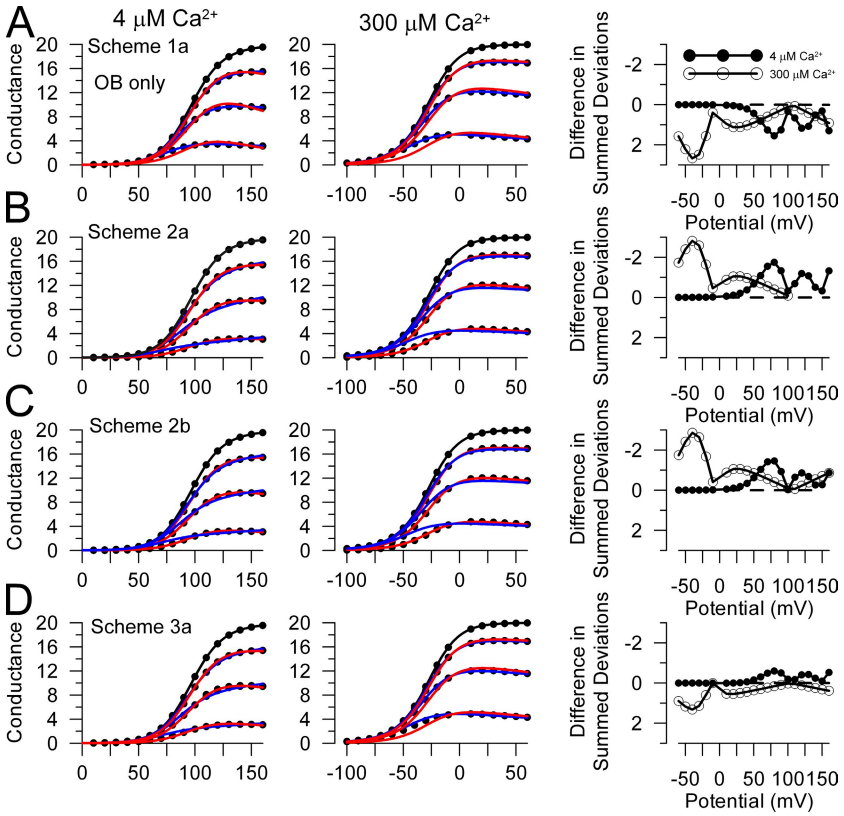

Figure 3. Models in which block is coupled to voltage sensor movement can account for differential ability of OB and CB–OB models to fit data at low and high Ca^{2+}. (A) GV curves were generated with Scheme 1a, both with 4 μM Ca^{2+} (left) and 300 μM Ca^{2+} (middle). Simulations were done with nominal blocker concentrations of 0.14-, 0.57-, and 2.86-fold the effective K_b. Blue lines correspond to the best fit of a strictly open-channel block model (Eq. 8 with W = 100,000), and red lines correspond to the best fit of a completely state-independent CB–OB model (Eq. 8 with W = 1). On the right, the difference between OB–CB (Eq. 8 with W = 1) summed residuals measured for all [bbTBA] at each voltage and the OB summed residuals (W = 100,000) is plotted as a function of voltage. Points on the upper half of such plots indicate that the fit of the OB model (W = 100,000) yielded larger deviations than the W = 1 assumption. In this case, W = 1 yielded poorer fits both at 4 (filled circles) and 300 μM (open circles). (B) GV curves were generated from currents simulated using Scheme 2a ($K_{bo} = K_{bc}$ and $z_o = z_c$). In this case, the W = 1 assumption fits the GV curves better at both 4 and 300 μM. (C) GV curves were generated with Scheme 2b ($z_c = 0\ e$) and fit as above. Again, the CB–OB equation provides a better fit both at 4 and 300 μM Ca^{2+}. (D) GV curves were generated with Scheme 3a ($K_{bo} = K_{bc}$ and $z_o = z_c$) and fit as above. The right-hand panel indicates that the GV curves at 4 μM were somewhat better fit with the CB–OB model, whereas at 300 μM, the standard OB model provided a better fit. Similar results were obtained with Scheme 3b ($z_c = 0\ e$).

We next relaxed the constraints that $K_{bc} = K_{bo}$ and $z_o = z_c$, and GV curves were fit with Schemes 2 and 3 with K_{bc}, K_{bo}, z_o, and z_c, with all allowed to vary independently (Fig. 4, D and E). With all block parameters unconstrained, Schemes 2 and 3 each gave very reasonable fits of the GV curves. The deviations (SSQ/pt) that arose solely from the GVs obtained in bbTBA were 0.00925 (Scheme 3) and 0.010225 (Scheme 2), corresponding to an ~10% increase in quality of fit with Scheme 3 relative to Scheme 2.

Despite the overall adequacy of the fits for both models (Fig. 4, D and E), we were concerned about the physical plausibility of the actual parameter values. In particular, in each case, the best fit required that z_c, the voltage dependence of closed-channel block, be rather large, with 0.8 e for Scheme 2 and 0.44 e for Scheme 3. Voltage dependence in closed-channel block cannot be excluded out of hand and, in fact, calculations based on physical dimensions of the KcsA open- and closed-channel structures (Roux et al., 2000) suggest that the effective field will extend farther into the central cavity from the selectivity filter in closed channels. However, a potential issue when $z_c > z_o$ is that, in a full allosteric scheme in which microscopic reversibility is assumed, a pronounced voltage dependence of closed-channel block requires a very pronounced voltage-dependent effect on the CB–OB transition (see Scheme 6 for one blocking tier in which voltage dependence is split evenly within the CB–OB transition). In Scheme 6, $K_{bo}(V) = (k_r/k_f)\exp(-0.1V/kT)$, $K_{bc}(V) = (k_r/k_f)\exp(-0.8V/kT)$, with $L(V) = \delta(V)/\gamma(V)$. If one requires that microscopic reversibility be maintained, a voltage dependence equivalent to the difference in the voltage dependence of closed- versus open-channel block must be distributed between transitions in the CB←→OB equilibrium. When such voltage dependence is distributed identically to both the channel-opening and -closing transitions, this predicts strong slowing effects on macroscopic current activation and deactivation kinetics (Fig. S5), which are inconsistent with the observed effects of bbTBA on gating kinetics (Figs. 1 and 8 for activation and Fig. 13 for deactivation). In fact, regardless of how voltage dependencies are distributed to the CB–OB transitions in Scheme 6, as long as microscopic

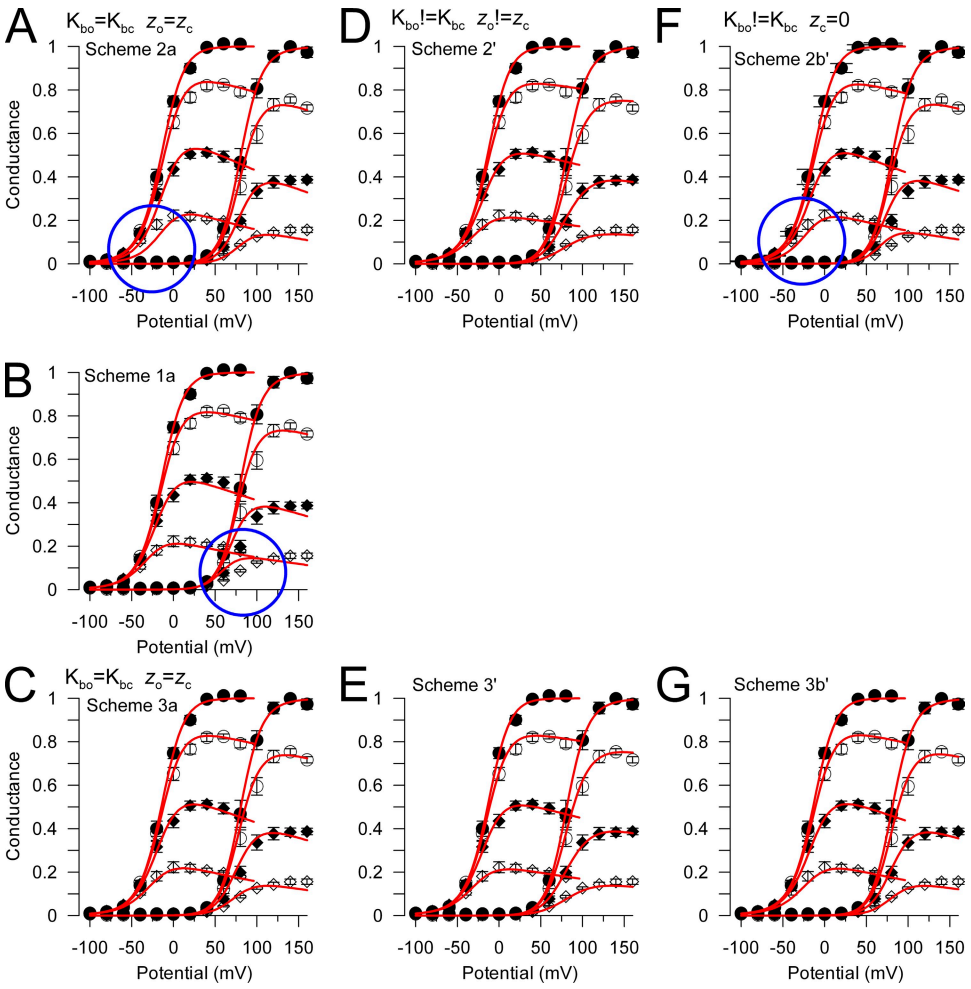

Figure 4. Coupling block of closed and open states to voltage sensor movement improves fit of GV curves at both 4 and 300 μM Ca^{2+}. (A) GV curves were generated from steady-state currents in a set of patches in which the blocking effects of 0, 1, 5, and 20 μM bbTBA were examined at both 4 and 300 μM. The full set of GV curves was then fit to Eq. 13, corresponding to a block with a completely state-independent blocking scheme (2a) for channels activated in accordance with a full allosteric activation scheme (Horrigan and Aldrich, 2002). Scheme 2a provides a poor fit (SSQ = 0.0417/pt) to the GV curves, particularly at 20 μM bbTBA and 300 μM Ca^{2+} (blue circle). $K_{bc} = K_{bo} = 7.48 \pm 0.43$ μM ($z_c = z_o = 0.17 \pm 0.02$ *e*). (B) GV curves were fit with the open-channel block model (Eq. 12; Scheme 1a). $K_{bo} = 5.94 \pm 0.39$ μM ($z_o = 0.13 \pm 0.02$ *e*); SSQ/pt = 0.0525. Deviations between the data and the fit are particularly apparent at 20 μM bbTBA and 4 μM Ca^{2+} (blue circle). (C) The GV curves were fit with Eq. 14 for Scheme 3a, in which block depends on movement of at least one voltage sensor. $K_{bo} = K_{bc} = 6.36 \pm 0.27$ μM ($z_o = z_c = 0.14 \pm 0.01$ *e*), with SSQ/pt = 0.0219. For D–I, fitted curves correspond to schemes in which $K_{bo} \neq K_{bc}$. In D and E, both z_o and z_c varied independently, whereas in F and G, $z_c = 0.0$ *e*. (D) For Scheme 2′, the best fit to the GV curves yielded $K_{bo} = 6.00 \pm 0.3$ μM, $z_o = 0.095 \pm 0.02$ *e*, $K_{bc} = 45.8 \pm 35.9$ μM, and $z_c = 0.81 \pm 0.21$ *e*, with SSQ = 0.0140/pt. (E) For Scheme 3′, $K_{bo} = 6.01 \pm 0.27$ μM, $z_o = 0.10 \pm 0.02$ *e*, $K_{bc} = 8.1 \pm 6.7$ μM, and $z_c = 0.44 \pm 0.23$ *e*, with SSQ = 0.0131/pt. (F) For Scheme 2b′, with z_c constrained to 0 *e*, $K_{bo} = 6.36 \pm 0.45$ μM, $z_o = 0.15 \pm 0.02$ *e*, and $K_{bc} = 21.4 \pm 12.2$, with SSQ = 0.0453/pt. The blue circles highlight the poorly fit region. (G) For Scheme 3b′, $z_c = 0$ *e*, $K_{bo} = 6.48 \pm 0.29$ μM, $z_o = 0.13 \pm 0.01$ *e*, and $K_{bc} = 2.34 \pm 0.38$, with SSQ = 0.0192/pt.

reversibility is maintained, the net effect is to alter some aspect of activation or deactivation kinetics in a fashion that contradicts observation.

$$\begin{array}{ccc} C & \underset{k_r \exp^{0.4V/kT}}{\overset{k_f \exp^{0.4V/kT}}{\rightleftharpoons}} & CB \\ \downarrow\uparrow \frac{\exp^{0.212V/kT}}{\exp^{.088V/kT}} & & \downarrow\uparrow \frac{\exp^{0.138V/kT}}{\exp^{0.262V/kT}} \\ O & \underset{k_r \exp^{0.05V/kT}}{\overset{k_f \exp^{0.05V/kT}}{\rightleftharpoons}} & OB \end{array}$$

(SCHEME 6)

We next considered the case in which closed-state block is completely voltage independent (Fig. 4, F and G). With this assumption and one less free parameter, the fit of Scheme 3b′ was quite a bit better than for Scheme 2b′, with the deviations (SSQ/pt) arising from the GV curves in bbTBA being 0.0154 (Scheme 3) and 0.0415 (Scheme 2).

Overall, this comparison of the ability of Schemes 2 and 3 to fit the GV curves at low and high Ca^{2+} indicates that a model in which the resting closed state is unblocked by bbTBA provides a better description of the data than a model in which bbTBA blocks all closed states. Although we have considered the consequences of different assumptions for the voltage dependence of closed-channel block, the analysis does not allow strong conclusions regarding z_c, except that, if microscopic

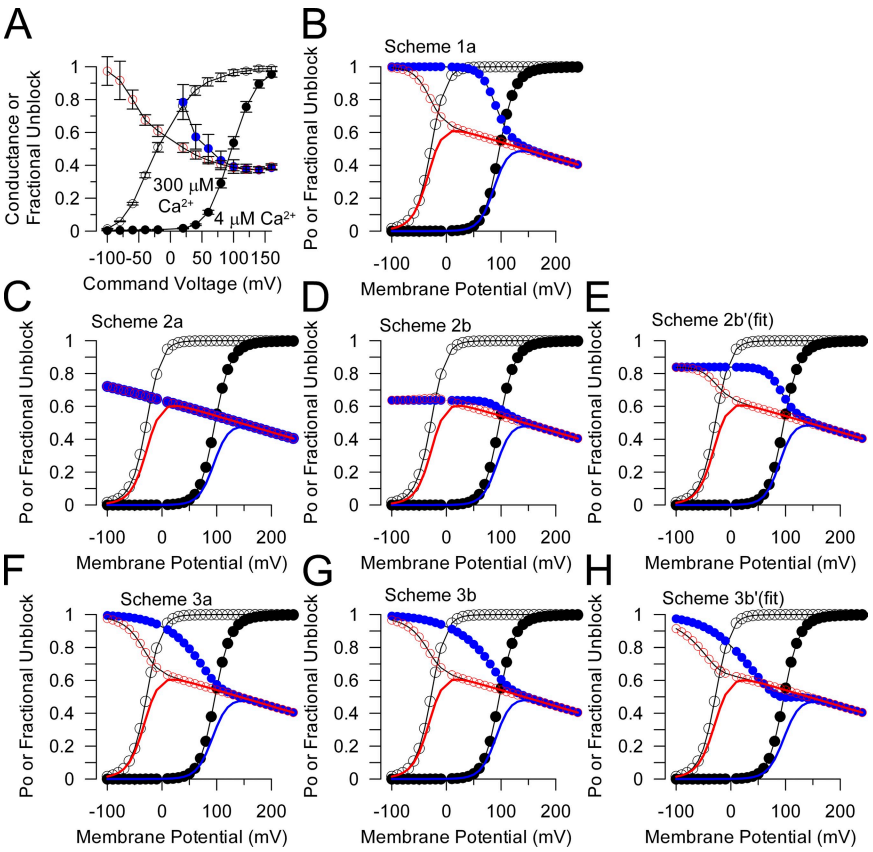

Figure 5. Differences in fractional unblock of BK channels by bbTBA between 4 and 300 μM Ca^{2+} are not supportive of fully state-independent block. (A) From measurements of macroscopic conductance (Fig. 1), the fractional unblock (=G(bbTBA/G(control)) with 5 μM bbTBA was determined over the full range of voltages for both 300 μM Ca^{2+} (red circles) or 4 μM Ca^{2+} (blue circles) and compared with GVs for current activation. Over the range of +20 to +60 mV, the fractional unblock at 4 μM Ca^{2+} is larger than that for 300 μM Ca^{2+}, whereas fractional unblock with 300 μM Ca^{2+} approaches 1.0 at the most negative activation voltages. (B) Predictions for simple open-channel block (Scheme 1a) are illustrated. GV curves at 4 (open circle) and 300 (closed circle) μM Ca^{2+} are plotted along with GV curves in the presence of bbTBA (blue with 4 μM Ca^{2+} and red with 300 μM Ca^{2+}). Fractional unblock is also plotted for 4 μM (blue circle) and 300 μM (red circle) at each voltage. (C) Similar plots for currents generated with Scheme 2a show that fractional unblock is identical for both 4 and 300 μM Ca^{2+} at each voltage. (D) The relationships for Scheme 2b, in which closed-channel block is voltage independent, are shown. The limiting fractional unblock at negative voltages reflects the voltage independence of closed-channel block. (E) Block and fractional unblock were determined from currents simulated using blocking constants derived from simultaneous fitting of GV curves to Scheme 2b (Fig. 4 G, with K_{bc} of ~3 K_{bo}). (F) Predictions derived from currents simulated with Scheme 3a are plotted. (G) Predictions based on Scheme 3b (z_c = 0.0 *e*) are plotted. (H) Predicted block and fractional unblock are shown based on currents simulated with blocking constants from simultaneous fitting of GV curves to Scheme 3b (Fig. 4 H, with K_{bo} = 3 K_{bc}).

reversibility is assumed, z_c is unlikely to be greater than z_o. We now address whether other details of block by bbTBA may help discriminate among various closed-state blocking models.

Model dependence of fractional unblock at low and high open probabilities

An important result supporting the idea that bbTBA blocks both closed and open channels in a state-independent fashion was the demonstration that the fractional unblock of single BK channels either at low or high Ca^{2+} was largely independent of channel Po (Wilkens and Aldrich, 2006). Fractional unblock corresponds to the fraction of BK current that remains unblocked at given bbTBA and activation conditions. For state-independent block, the fraction of unblocked channels will be identical under all conditions of channel activation.

Using the GV curves in Fig. 1, we determined fractional unblock at 4 and 300 μM Ca^{2+} with 5 μM bbTBA (Fig. 5 A). Estimates of fractional unblock for Po values >~0.4 obtained with 4 μM Ca^{2+} overlapped estimates of fractional unblock obtained with 300 μM Ca^{2+}. This is generally consistent with the earlier observations of Wilkens and Aldrich (2006), in which fractional unblock for different [Ca^{2+}] was only compared at relatively high Po. However, our estimates of fractional unblock obtained at Po < 0.4 with 4 μM Ca^{2+} exhibited marked deviations from the fractional unblock obtained at identical voltages with 300 μM Ca^{2+}. This was true at multiple bbTBA concentrations (not depicted). Furthermore, the fractional unblock with 300 μM Ca^{2+} exhibited a clear upward curvature in unblock at lower open probabilities. The differences between our results and those of Wilkens and Aldrich may reflect the more limited range of estimates at lower Po provided in the earlier study. Based on Fig. 5 A, two aspects of these fractional unblock relationships contradict the expectations of a completely state-independent blocking scheme: first, the difference in fractional unblock observed at low and high Ca^{2+} over some voltages and, second, the upward curvature in unblock observed at 300 μM Ca^{2+}.

To compare predictions of different models, we determined fractional unblock from the GV curves generated

by different blocking schemes (Fig. 5, B–H). With Scheme 1a (Fig. 5 B; simple open-channel block), fractional unblock is identical at 4 and 300 μM Ca^{2+} over Po values for 4 μM above ∼0.6. Below 0.6, the fractional unblock curves exhibit marked differences, although both approach 1.0 at low Po values. In contrast, for the fully state-independent Scheme 2a (Fig. 5 C; $K_{bo} = K_{bc}$ and $z_c = z_o$), the fractional unblock curves at 4 and 300 μM completely overlap as expected (Wilkens and Aldrich, 2006). However, when $z_c = 0$ *e* as in Scheme 2b (Fig. 5 D), deviations between fractional unblock are observed at lower and higher Ca^{2+}, with both reaching an asymptote at negative voltages corresponding to the voltage-independent K_{bc}. The fractional unblock predictions based on fitted values for Scheme 2b′ (Fig. 4 F; $K_{bo} \neq K_{bc}$ and $z_c = 0$ *e*) also showed discrepancies between fractional unblock at lower and higher Ca^{2+} (Fig. 5 E) For models with block coupled to voltage sensor movement (Fig. 5, F–H), the differences between fractional unblock curves at 4 and 300 μM Ca^{2+} tend to be intermediate between those observed for Schemes 1a and 2a. However, in all cases, fractional unblock approaches 1 at the lowest Po values both for low and high Ca^{2+}. This reflects the fact that the fully resting closed state is not subject to block by bbTBA in these models. It is also noteworthy that, for all the variants of Scheme 3 shown in Fig. 5 (F–H), the fractional unblock curves for 4 and 300 μM overlap down to a Po at 4 μM of ∼0.5.

These considerations indicate that a variety of models that incorporate closed-channel block, but are not strictly state independent, can produce the correspondence of fractional unblock over the ranges previously examined by Wilkens and Aldrich (2006). Given challenges (small currents and large variance) that arise in the estimates of fractional unblock obtained at low Po for lower [Ca^{2+}], the datasets used for this type of analysis may have limitations for rigorous model discrimination. However, the clear tendency of fractional unblock at 300 μM to approach 1.0 and the discrepancies between fractional unblock at 4 and 300 uM Ca^{2+} over the range of low Po in 4 μM Ca^{2+} (Fig. 5 A) suggest that the fully state-independent version of Scheme 2 is not consistent with observations.

Another important component of the analysis of Wilkens and Aldrich (2006) was an examination of the Po dependence of fractional unblock. Although their observation that similar fractional unblock with bbTBA is observed at both low and high Po over a range of voltages is consistent with the expectations of state-independent block (Fig. 6 A), we have found that this behavior could also be reproduced by Scheme 3 (Fig. 6, D–F), dependent on particular parameters for block of open and closed states. Scheme 3a (Fig. 6 D) predicts a difference in fractional block at low and high Po that is intermediate between that for open-channel block (Fig. 6 A, 1a) and Scheme 2a. For schemes in which $K_{bc} = K_{bo}$, but $z_c = 0$ *e*, there is an additional increase in slope in the fractional block versus Po relationship (Fig. 6, B, Scheme 2b, and E, Scheme 3b). Interestingly, the fractional unblock versus Po relationship based on the fitted values ($z_c = 0.0$ *e* and $K_{bc} \neq K_{bo}$) from Fig. 4 G for Scheme 3 results in relatively Po-independent estimates of fractional unblock (Fig. 6 F). This indicates that the absence of detectable slope in the fractional unblock

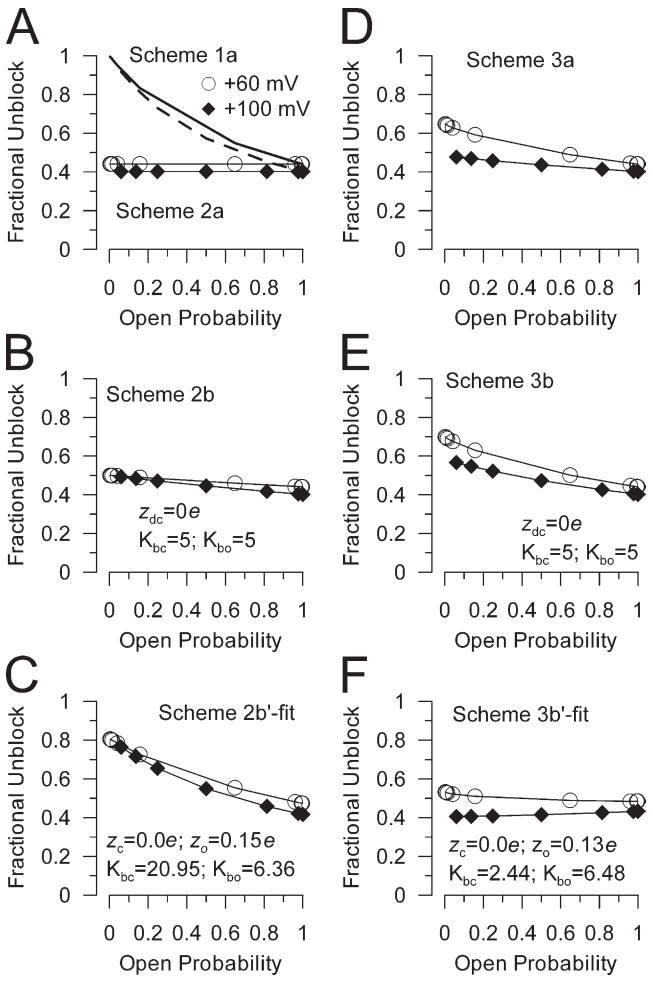

Figure 6. The dependence of fractional unblock on Po may not discriminate among various state-dependent blocking models. Fractional unblock was determined based on generation of families of Po versus voltage curves over a range of Ca^{2+} assuming various blocking schemes. (A) Dotted and solid lines correspond, respectively, to dependence of fractional unblock on Po for +60 and +100 mV, based on the open-channel block model given by Scheme 1a. Filled and open circles correspond to predictions based on Scheme 2a at +100 and +60 mV, respectively. (B) For Scheme 2b, fractional unblock exhibits a slight dependence on Po. (C) For Scheme 2b′, based on values derived from the fit of GV curves (Fig. 4 G), fractional unblock exhibits a strong dependence on Po. (D) Fractional unblock is plotted as a function of Po for Scheme 3a. (E) Fractional unblock is plotted as a function of Po for Scheme 3b. (F) Fractional unblock is plotted as a function of Po based on fitted values for Scheme 3b′ (Fig. 4 H), exhibiting largely Po-independent fractional unblock.

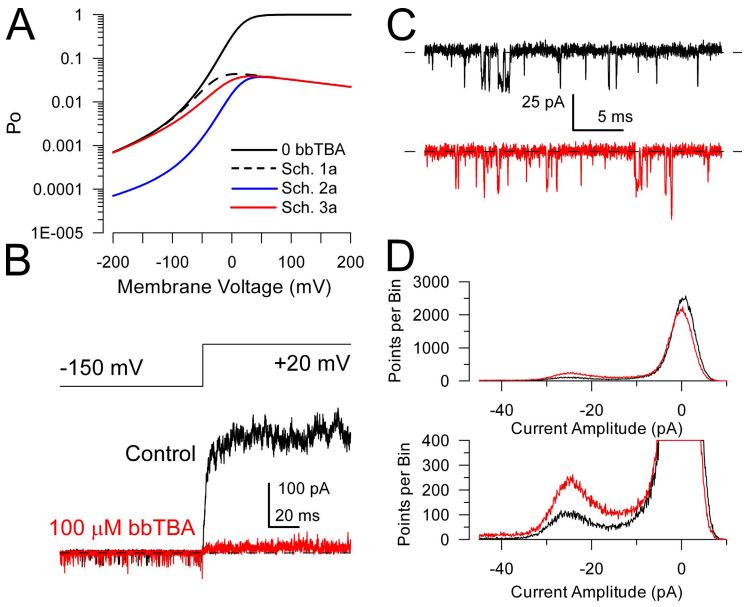

Figure 7. 100 µM bbTBA has no inhibitory effect on NPo at voltages over which voltage sensor activation is minimal. (A) Po-V curves are plotted based on a full Horrigan-Aldrich activation scheme for 30 µM Ca^{2+} (black line) along with predictions for block in the presence of 100 µM bbTBA for either Scheme 1a (open-channel block; dotted line), Scheme 2a (state-independent block; blue line), or Scheme 3a (block dependent on voltage sensor movement; red line). The state-independent Scheme 2a predicts the same percent block at positive potentials and at potentials where voltage sensors are inactive, whereas Schemes 1a and 3a predict no change in NPo when voltage sensors are inactive. (B) Channel openings were monitored with 30 µM Ca^{2+} at −150 mV before a step to +20 mV either in the absence (black) or presence (red) of 100 µM bbTBA. 100 µM bbTBA produces >90% block of BK current at +20 mV, with minimal obvious effect at −150 mV. (C) Expanded time base records from the traces in B are shown during the periods at −150 mV. (D) Histograms of the current amplitudes of all digitized time points during the recording at −150 mV in the absence (black) and presence (red) of 100 µM bbTBA are plotted, with the bottom panel showing the same data on a different scale. bbTBA results in an increase in NPo in this patch.

versus Po relationship does not allow a definitive test of whether a fully state-independent block model applies. Furthermore, it can be seen that a model in which block is dependent on voltage sensor activation is able to produce a Po independent of fractional unblock, similar to that observed for fully state-independent block.

bbTBA does not decrease NPo at negative potentials

The results of Fig. 5 A indicate that bbTBA may not produce the same fractional block at all open probabilities. We reasoned that, if block of BK channels by bbTBA does exhibit state dependence, this issue could best be tested by an examination of BK channel Po at very negative activation potentials. At potentials negative to about −120 mV, voltage sensors are predominantly inactive and BK Po is very low (Horrigan and Aldrich, 2002). In patches with a large number of channels, it is possible to measure NPo for channels with inactive voltage sensors and thus test the effects of bbTBA on NPo. In Fig. 7 A, the predictions for log(NPo) as a function of voltage are displayed for BK conductance at 30 µM Ca^{2+}, along with the predictions for changes in log(NPo) with 100 µM bbTBA in accordance with open-channel block (Scheme 1a), state-independent block (Scheme 2a), or block dependent on voltage sensor movement (Scheme 3a). Whereas Scheme 2a predicts a similar fractional reduction in NPo at all voltages, both Scheme 1a and Scheme 3a predict no reduction in Npo at potentials where voltage sensors are inactive. 100 µM bbTBA was chosen for this evaluation because, based on the 0-voltage K_b for block of open and/or closed BK channels by bbTBA (∼5 µM) and its voltage dependence (z ∼0.1 *e*), we predict that 100 µM bbTBA should be at least 10 times the predicted K_d (∼9.05 µM) at −150 mV. Thus, examination of NPo at negative potentials should provide a direct test for the idea that channels with resting voltage sensors may be insensitive to bbTBA.

In our experiments, patches were held at −150 mV with 30 µM Ca^{2+} to help elevate NPo. Under these conditions, voltage sensors remain inactive (Horrigan and Aldrich, 2002). A brief activation step to +20 mV was used to provide a measure of the total net BK conductance in the patch and to confirm the sensitivity of BK current to bbTBA under conditions where voltage sensors are activated. Example traces in Fig. 7 B show the marked inhibition of current at +20 mV by 100 µM bbTBA, with little obvious effect on channel activity at −150 mV. Expanded time base records of channel activity at −150 mV (Fig. 7 C) reveal no obvious decrease in overall NPo. In fact, total amplitude histograms of current levels recorded at −150 mV reveal a small increase in NPo in the presence of 100 µM bbTBA (Fig. 7 D). Similar increases in NPo were observed in four other patches tested with 100 µM bbTBA at −150 mV. Although we not know the basis for the increase in NPo, the results show that blockade by bbTBA is markedly reduced at −150 mV relative to that occurring at voltages where voltage sensors are active (e.g., at +20 mV over 90% block in Fig. 7 B). In contrast, the state-independent blocking model predicts a much smaller difference in reduction in NPo between −150 and −20 mV. Specifically, with a voltage dependence of block of 0.1 *e* and low Po, the fractional reduction in NPo in the presence of bbTBA should be only about twofold less at −150 mV than at +20 mV. Although it might be suggested that the bbTBA-elicited increase in NPo almost

exactly balances a simultaneous blocking effect, to mask such a blocking effect would require that 100 µM bbTBA produce an ~10-fold increase in NPo at negative potentials. We consider this unlikely and arguments against this possibility are presented in the Discussion. We therefore interpret the absence of a bbTBA-mediated decrease in NPo at negative potentials as strong evidence that bbTBA block is not state independent and, furthermore, that closed channels with inactive voltage sensors are resistant to block by bbTBA.

Ca^{2+} and voltage dependence of triphasic relaxations in bbTBA

Slow kinetic aspects of the onset of bbTBA block were exploited by Wilkens and Aldrich to argue that bbTBA blocks both closed and open channels. Specifically, after depolarization, bbTBA can produce a rapid time-dependent block of BK channels that is subsequently followed by a small undershoot of current before a steady-state level of current is achieved (Wilkens and Aldrich, 2006). Here, we provide additional examination of the activation conditions leading to observation of the triphasic relaxations and, furthermore, show that this behavior is not unique to the fully state-independent blocking scheme.

The triphasic waveform cannot arise from an exclusively open-channel block model (Wilkens and Aldrich, 2006), but requires some block of both closed and open channels (also see Fig. 2). Not unexpectedly, the triphasic behavior depends on a particular set of activation conditions (voltage and Ca^{2+}) and bbTBA concentrations that allows separation of the activation kinetics and block kinetics. The triphasic waveform was readily observed with channels activated by 10 µM Ca^{2+} in the presence of 75 µM bbTBA (Fig. 8 A). At 4 µM Ca^{2+}, some triphasic behavior was observed (Fig. 8 B), although this was diminished by the extent to which block approaches steady state before the peak of current activation. At 300 µM, there was essentially no sign of the undershoot in current (Fig. 8 B), presumably because both activation and block reach equilibrium during the initial decay of current.

We next compared the ability of different models to reproduce the general features of the triphasic relaxations. Fig. 9 compares simulated currents obtained with voltage steps from +120 to +240 mV at both 4 and 300 µM Ca^{2+} with an effective blocker concentration of ~6*K_{bo}. We first compared the cases in which $K_{bo} = K_{bc}$ and $z_o = z_c$. Simulated currents resulting from Schemes 2a (Fig. 9 B) and 3a (Fig. 9 E) exhibit clear triphasic relaxations at 4 µM Ca^{2+}, similar to actual BK currents (Fig. 9 A), with no triphasic relaxation at 300 µM. In the examples shown, z_o and z_c were set to 0.2 *e* for Scheme 2a and 0.1 *e* for Scheme 3a because for Scheme 2a, the triphasic relaxation was not as obvious with $z_o = z_c = 0.1$ *e*. We also compared Schemes 2b and 3b, in which $z_c = 0.0$ *e*,

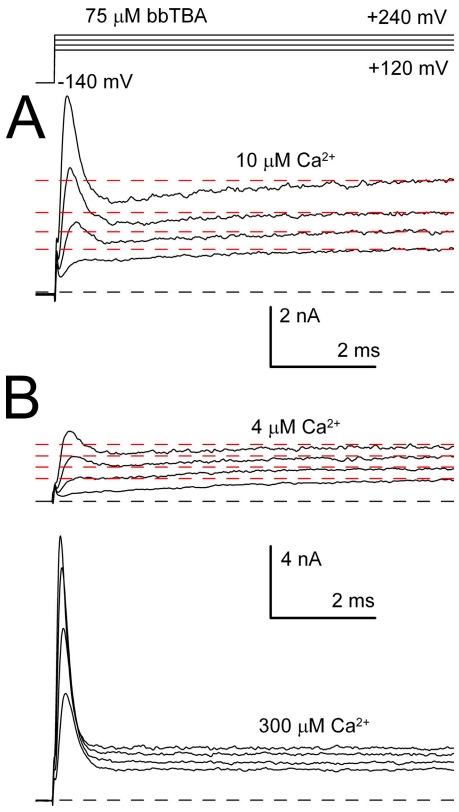

Figure 8. Block by bbTBA results in complex multicomponent relaxations. (A) Currents were activated with the indicated voltage protocol (top), with 10 µM Ca^{2+} in the presence of 75 µM bbTBA. Each trace is the average of 30 individual runs. Dotted red lines indicate the average current level at the end of each voltage step to highlight the marked undershoot that can occur after the initial rapid onset of block. (B) In a different patch, the same voltage protocol was used to activate BK currents either with 4 (top) or 300 µM Ca^{2+} (bottom), in both cases with 75 µM bbTBA. At 4 µM, dotted lines indicate steady-state current levels to highlight the undershoot after initial rapid block. With 300 µM Ca^{2+}, no undershoot is observed.

whereas $K_{bo} = K_{bc}$. In this case, triphasic relaxations were abolished for Scheme 2b (Fig. 9 C), while persisting for Scheme 3b (Fig. 9 F). Adjustments of parameters of block within the context of Scheme 2b failed to reveal conditions producing a triphasic relaxation. The difference between Schemes 2a, 2b, 3a, and 3b in producing triphasic relaxations is highlighted in Fig. S6. This outcome argues strongly that a blocking scheme in which all closed states can be blocked by bbTBA, but closed-channel block is voltage independent, is inconsistent with experimental observations. We also compared current simulations using parameters of block obtained from the fits in Fig. 4 (F and G), where $z_c = 0.0$ *e*, but $K_{bo} \neq K_{bc}$. Again, the simulations based on Scheme 2 (Fig. 9 D) fail to exhibit triphasic relaxations, whereas those based on Scheme 3 (Fig. 9 G) exhibit triphasic relaxations. Overall, none of the schemes and sets of

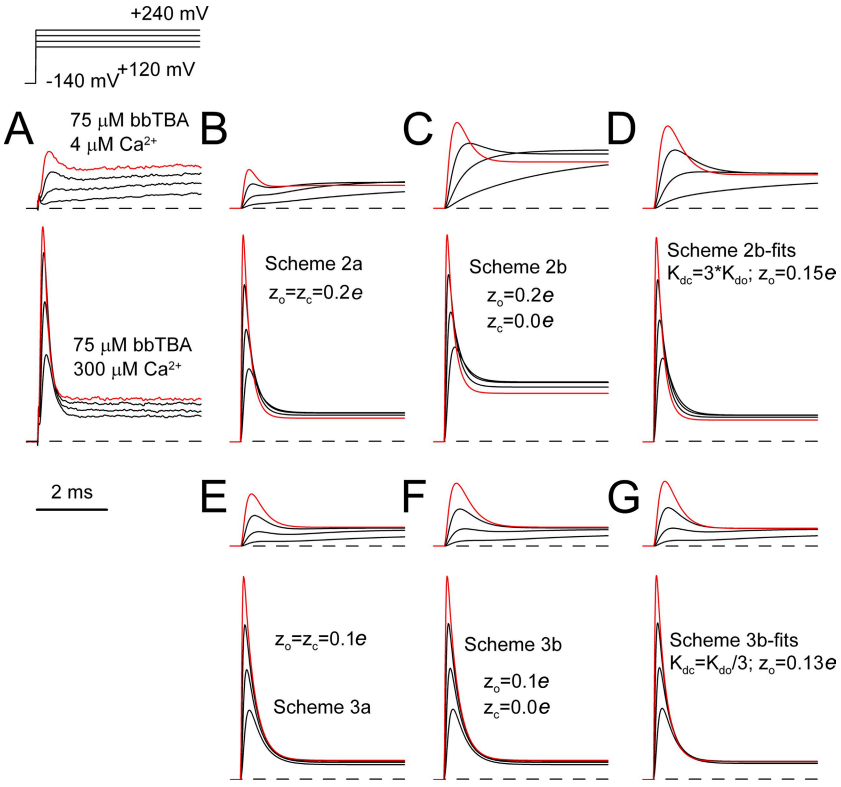

Figure 9. Triphasic relaxations arise from closed-channel block, but do not clearly distinguish among different models of closed-channel block. (A) These traces replot Fig. 8 A to allow comparison to simulated currents. Red traces correspond to +240 mV. (B) Currents were simulated using Scheme 2a with activation rates given in Table I, with the effective [blocker] = 5.71 * K_{do}, with $z_o = z_c = 0.2$ *e*. Top traces correspond to 4 μM Ca^{2+} and the bottom traces to 300 μM. When $z_o = z_c = 0.1$ *e*, the triphasic relaxations were not as obvious. (C) Currents were simulated with Scheme 2b with $z_c = 0.0$. No triphasic relaxations are observed. (D) Currents were simulated with Scheme 2b′ but with a ratio of K_{do}/K_{bc} based on fitted values from Fig. 4 F. Again, no triphasic relaxation is observed. (E) Currents were simulated with Scheme 3a with $z_o = z_c = 0.1$ *e*. (F) Currents were simulated with Scheme 3b ($z_o = 0.1$ *e* and $z_c = 0.0$ *e*). (G) Currents were stimulated with values corresponding to the fitted values of Scheme 3b′ from Fig. 4 G.

parameters we tested completely mimics all features of the experimental data. In particular, differences exist in regards to the relative change in steady-state current levels at different voltages and also in the relative magnitude of the initial time-dependent block at different [bbTBA]. However, this arises in part because the experimental data were collected with a 5-ms prepulse to −140 mV, whereas the simulations used a 20-ms prepulse that was found to better approximate a steady-state condition.

In principle, the distinctions among schemes in terms of the relative amplitudes of the three components in such relaxations might be used to evaluate whether one or the other scheme better approximates the actual behavior of bbTBA. However, practically, we have found it difficult to reliably measure such relaxations at high bbTBA over a range of voltages because robust sets of such relaxations require a large number of channels and/or averaging of a large number of runs. Thus, at this point we simply state that, when $z_o = z_c$, all schemes permit triphasic relaxations, whereas if $z_c = 0.0$ *e*, triphasic relaxations only occur in schemes (both Schemes 3 and 4) in which block is coupled to voltage sensor movement.

Fractional availability of BK channels in the presence of bbTBA

Given that bbTBA blocks both open and at least some closed channels, the peak current during a depolarization in the presence of bbTBA should reflect, in addition to the time course of block of open channels, the resting equilibrium between channels in C and CB states before depolarization. Varying the conditioning potential before depolarization might therefore be expected to provide some information regarding the voltage dependence of the C–CB equilibrium. We therefore examined the dependence of peak BK current in the presence of different [bbTBA] on conditioning potentials between −300 and +100 mV. We term this the fractional availability of BK channels, reflecting in part the relative occupancy of channels in closed-unblocked states. An example of such a protocol is shown in Fig. 10 A, with currents activated at 4 μM Ca^{2+}, a concentration at which there will be minimal occupancy of open or open-blocked states at potentials negative to −50 mV. Under these conditions, the component of BK current that exhibits time-dependent block in the presence of 20 μM bbTBA increases in amplitude as the conditioning potential is made more negative over the range of +100 mV to about −100 mV (Fig. 10, C and D). However, at more negative potentials, there is essentially no change in amplitude of the time-dependent current. With 75 μM bbTBA (Fig. 10 B), the block of BK current occurs more rapidly and more completely, but there is still little change in peak current amplitude at potentials negative to about −100 mV (Fig. 10, C and D), although the increase in bbTBA concentrations does produce a leftward shift in the voltage of half-availability (V_h).

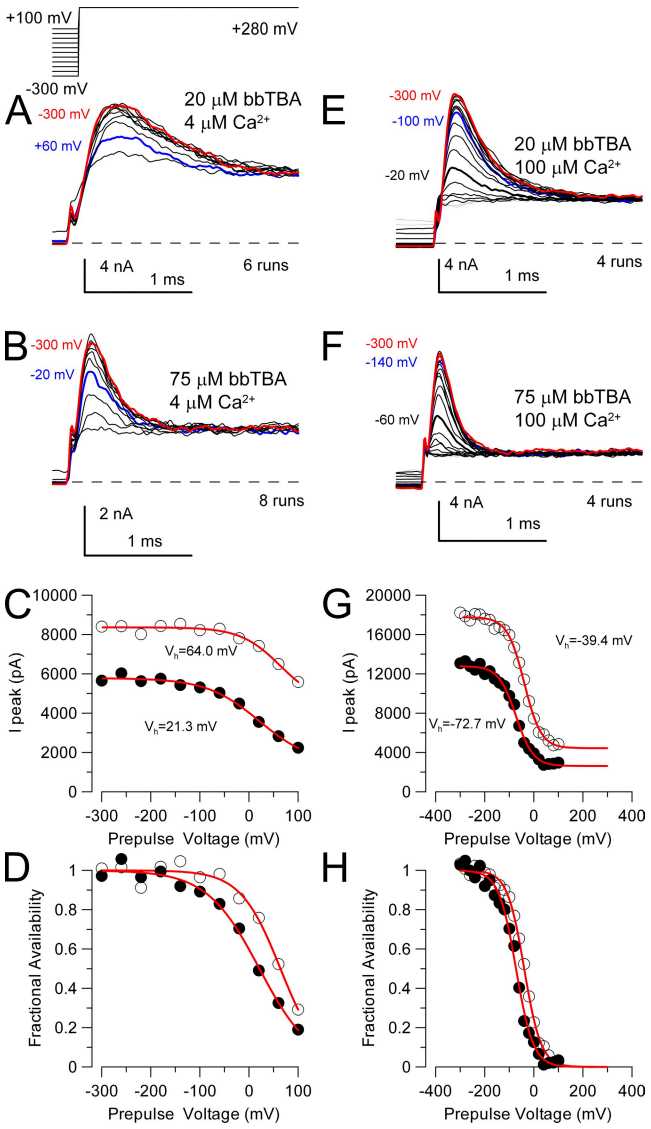

Figure 10. Fractional availability of current in the presence of bbTBA exhibits voltage independence at negative potentials. (A) Slo1 currents from excised inside-out patches were activated by the indicated voltage protocol (top; prepulse voltages from −300 to +100 mV with 40-mV increments) with 4 μM of internal Ca^{2+} and 20 μM bbTBA. The peak amplitude of the rapidly decaying current exhibits little change until prepulse voltages of 0 mV or more positive. Red trace corresponds to a −300-mV prepulse and blue to a +60-mV prepulse. (B) In the same patch, currents were activated with 4 μM Ca^{2+} along with 75 μM bbTBA. Red trace, −300-mV prepulse; blue trace, −20-mV prepulse. (C) The peak current amplitudes are plotted as a function of prepulse potential for both 20 μM (open circles) and 75 μM (filled circles) bbTBA. Red lines correspond to fits of a Boltzmann function with V_h = 64.9 ± 54.4 mV (z = 0.62 ± 0.33 *e*) and 22.9 ± 34.9 mV (z = 0.46 ± 0.13 *e*) for 20 and 75 μM bbTBA, respectively. (D) Normalized fractional availability was determined based on the fit of the Boltzmann function in C, better illustrating the leftward shift in availability with the increase in bbTBA. (E) The same protocol was used to activate currents in 100 μM Ca^{2+} (a different patch) with 20 μM bbTBA. The peak current at −100 mV (blue trace) shows some reduction compared with −300 mV (red trace). (F) The same patch was exposed to 75 μM bbTBA, producing more rapid and complete block. (G) The peak current is plotted as a function of prepulse potential either with 20 μM bbTBA (V_h = −39.4 ± 3.3 mV and z = 0.73 ± 0.06 *e*) or 75 μM bbTBA (V_h = −72.7 ± 4.5 mV and z = 0.72 ± 0.09 *e*). (H) The normalized fractional availability curves for the data in G are replotted.

The change in peak current amplitude as a function of prepulse potential was also examined for BK currents activated by 100 μM Ca^{2+} (Fig. 10, E and F). With 100 μM [Ca^{2+}], the reduction of peak current was shifted to more negative potentials, but at potentials from −140 to −300 mV, there was still little change in peak current amplitude (Fig. 10 G) or fractional availability (Fig. 10 H). The leftward shift in V_h with increases in Ca^{2+} is to be expected in conjunction with the leftward shift in the activation curve for the BK channels. The dependence of peak current on prepulse voltage was fit with a Boltzmann function with values given in the legend to Fig. 10. An increase either in [Ca^{2+}] or in [bbTBA] shifts the availability curves leftward.

Well-defined half-availability curves were difficult to achieve, even with the averaging of many runs, because of the stochastic variability in the peak current amplitude. To better define such curves, we examined availability with prepulse voltages from −300 to −100 with larger numbers of runs in one set of patches, while in another set we examined voltages from −200 to +100 (+150 mV with 4 μM Ca^{2+}) mV. This allowed a larger number of sweeps and the use of 20-mV increments in conditioning potentials. Fractional availability curves covering the range of −300 to +150 mV were generated by normalizing the curves at overlapping voltages (Fig. 11). At 4 μM Ca^{2+}, with either 20 or 75 μM bbTBA, the range of voltages over which changes in fractional availability of BK current occurs exhibits substantial overlap with the activation curve obtained under the same [Ca^{2+}] concentrations (Fig. 11 A), with a leftward shift in fractional availability with increases in [bbTBA]. The magnitude of the voltage dependence of the fractional availability (for 20 μM bbTBA, z = 0.76 ± 0.22 *e*, for 75 μM bbTBA, z = 0.59 ± 0.01 *e*) is less than that observed for the voltage dependence of activation by Ca^{2+} (q = 1.32 ± 0.07 *e*) but much greater than the ∼0.1 *e* observed for block of macroscopic steady-state current by bbTBA (e.g., Fig. 1). This suggests that the voltage dependence of availability of BK channels contributing to the peak transient current may be defined by the voltage dependence of transitions involved in channel activation, rather than channel block. With 100 μM Ca^{2+}, the fractional availability curves at 20 and 75 μM are shifted leftward relative to those at 4 μM (Fig. 11 B). Again, the voltage dependencies of the fractional availability curves (20 μM bbTBA, z = 0.88 ± 0.03 *e*, 75 μM bbTBA, z = 0.80 ± 0.02 *e*) are similar to that of the voltage dependence of activation (q = 0.98 ± 0.04 *e*), while greatly exceeding that of macroscopic steady-state current block (z = ∼0.1 *e*).

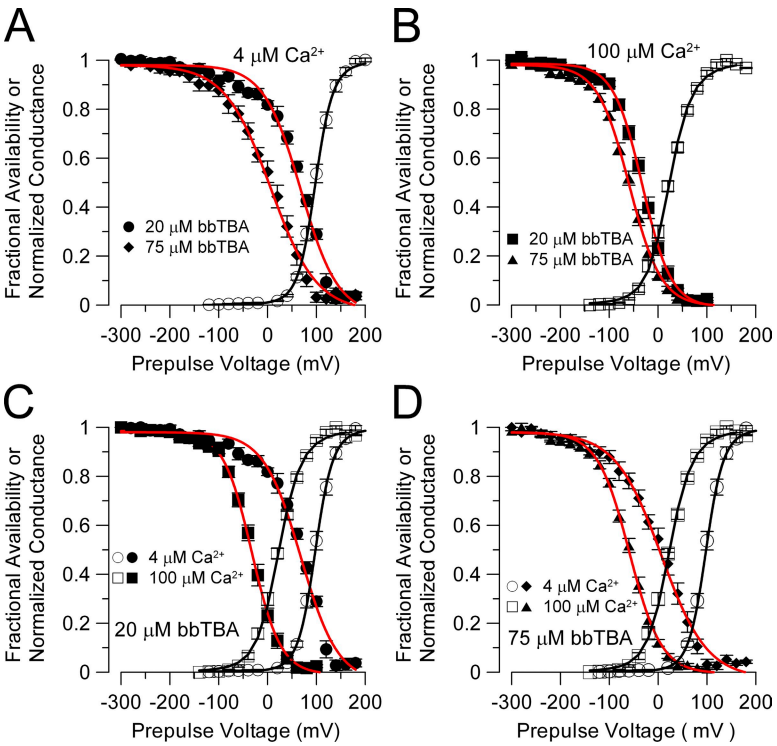

Figure 11. Dependence of BK fractional availability during bbTBA block on [Ca^{2+}] and [bbTBA]. (A) Currents were activated with 4 μM of internal Ca^{2+}. Control GV curves in the absence of bbTBA were generated from tail currents (open circles), and then fractional availability was determined either with 20 μM (filled circles) or 75 μM (diamonds) bbTBA using the protocol shown in Fig. 9. For 20 μM bbTBA, V_h = 67.1 ± 3.6 mV with z = 0.76 ± 0.02 *e*, whereas for 75 μM bbTBA, V_h = 5.1 ± 3.9 mV with z = 0.59 ± 0.01 *e*. The activation GV yielded V_h = 97.7 ± 0.7 mV (q = 1.32 ± 0.07 *e*). (B) Fractional availability and activation were defined in patches bathed with 100 μM of internal Ca^{2+}. With 20 μM bbTBA (filled squares), V_h = −32.6 ± 1.33 mV (z = 0.88 ± 0.03 *e*) and, for 75 μM bbTBA (filled triangles), V_h = −58.4 ± 1.4 mV (z = 0.80 ± 0.02 *e*). The activation GV (open squares) yielded V_h = 22.7 ± 1.15 mV (q = 0.98 ± 0.04 *e*). For each condition, five to six patches were used. (C) Curves from A and B are replotted to show the shift in fractional availability with 20 μM bbTBA as [Ca^{2+}] is increased from 4 to 100 μM. (D) Curves from A and B are replotted to show the shift in fractional availability with 75 μM bbTBA with increases in [Ca^{2+}] from 4 to 100 μM.

The shift in availability curves at a fixed [bbTBA] as Ca^{2+} is altered is highlighted in Fig. 11 (C and D, 20 μM bbTBA and 75 μM bbTBA, respectively). The availability curves shift in a Ca^{2+}-dependent fashion, indicating that the blocking events that limit the amplitude of the peak transient current must be state dependent.

These results allow two mutually exclusive interpretations. One possibility is that, if there is block of closed channels over the range of −120 to −300 mV, that block must be entirely voltage independent. If closed-channel block had a voltage dependence similar to open-channel block (∼0.11 *e*), a clear change in fractional availability would be expected over the range of −120 to −300 mV (see below). The second possibility is that there may be no block of BK channels in fully resting states. The latter interpretation is supported by the close overlap of the fractional availability curve with the activation curve and the similarities in voltage dependence, suggesting that changes in fractional availability are strongly coupled to states involved in channel activation, rather than direct block of closed channels.

Predictions for fractional availability exclude strict state-independent block by bbTBA

For each scheme, currents were simulated to allow determination of the voltage dependence of fractional availability (Fig. 12; also see Fig. S7). Simulated currents (both 4 and 300 μM Ca^{2+}) were activated by a depolarization to +200 mV after a conditioning voltage spanning the range of −400 to 100 mV (Fig. 12 A). Qualitatively, the completely state-independent Scheme 2a (Fig. 12 C) predicts a behavior that clearly distinguishes it from both the open-channel block of Scheme 1a (Fig. 12 B) as well as other schemes incorporating closed-channel block (Fig. 12, D–F). For Scheme 2a, as the conditioning potential is made more negative, the peak transient current activated at +200 mV increases continuously down through −400 mV. This reflects the fact that the fractional availability in Scheme 2a will be defined solely by the weak voltage dependence of the C–CB equilibrium of the channels with four inactive voltage sensors. In contrast, Schemes 3a and 3b (and 4a and 4b in Fig. S7) both exhibit saturation in fractional availability.

The fractional availability curves were plotted relative to activation GVs at nominal 4 μM Ca^{2+} (Fig. 12 G). When only open states can be blocked (Scheme 1a), the slope of the half-availability curve closely approximates the slope of the activation GV, whereas for strictly state-independent block (Scheme 2a), the slope of the half-availability curve reflects the voltage dependence of closed-channel block. For schemes in which block is coupled to activation of voltage sensors, the slope of the half-availability curves approaches that of the activation curves, and is clearly greater than that expected for the voltage dependence of either closed- or open-channel block. These model-specific availability curves place some constraints on the types of models that may account for the fractional availability curves obtained for expressed BK channels in the presence of bbTBA (Fig. 11). The fully state-independent Scheme 2a is clearly inconsistent with the observed data.

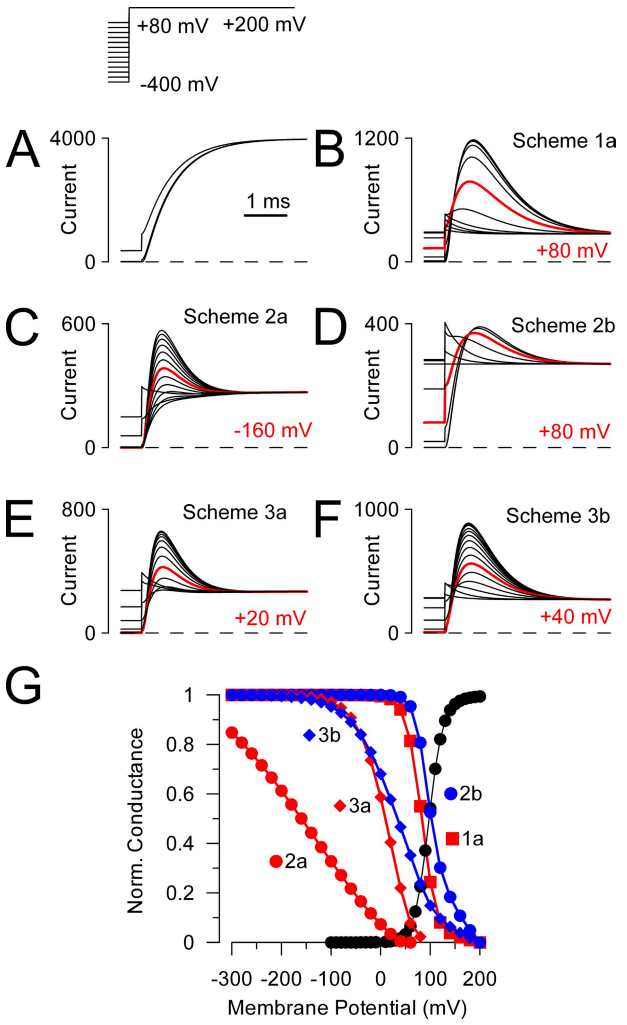

Figure 12. Fractional availability predictions for various models favor the idea that block of closed channels depends on voltage sensor movement. (A) Currents were simulated (10-state activation model) with the indicated voltage protocol (top left) for nominal 4 µM Ca^{2+} in the absence of blocker. Conditioning voltages were stepped in 20-mV increments, although for display purposes, only 40-mV increments are shown. (B) Currents were simulated with Scheme 1a, the open-channel block model. Red highlights traces (and voltage in red) in which the available fraction of current is ~0.5. Half-availability occurs near +80 mV, and at voltages negative to +40 mV, there is no additional increase in current availability. (C) Currents were simulated for Scheme 2a. No saturation in fractional availability is observed down through −300 mV. (D) Currents simulated with Scheme 2b exhibit saturation in fractional availability with half-availability around 60–80 mV. (E) Currents simulated with Scheme 3a showed half-availability near +20 mV with clear saturation. (F) Currents simulated with Scheme 3b showed half-availability near +40 mV with clear saturation. (G) The activation GV for 4 µM Ca^{2+} (filled black circles) is plotted along with normalized fractional availability curves for the peak transient currents for different schemes, as labeled. The voltage dependency of availability for Schemes 1a (red squares) and 2b (blue circles) yield values comparable in magnitude to that of activation (z of ~0.9 e). For Scheme 2a (red circles), the voltage dependence mirrors that of channel block (z of ~0.2 e). For Schemes 3a (red diamonds) and 3b (blue diamonds), the magnitude of the voltage dependence is less than that predicted for open-channel block, characteristic of bbTBA of Slo1 current.

Different block models also predict useful differences in the Ca^{2+} dependence of fractional availability curves. Models in which closed-channel block is coupled to voltage sensor movement (Schemes 3 and 4) exhibit Ca^{2+}-dependent shifts in the fractional availability curves (Fig. S7, F and H) because increased inactivation is favored by transitions involved in activation. In contrast, in any version of Scheme 2 in which block of all closed channels can occur, fractional availability becomes largely uncoupled from Ca^{2+} (Fig. 7 D) because availability becomes dominated largely by block of closed channels with inactive voltage sensors.

Modification of BK tail current decay by bbTBA depends on internal [Ca^{2+}]

Wilkens and Aldrich (2006) showed that 5 µM bbTBA produces little alteration in BK deactivation rates. Although this is generally consistent with the idea that blocked but open channels can close without blocker first dissociating from the channel, we find that the absence of tail current prolongation is not only predicted by state-independent block. Here, we examine BK tail currents in the presence of different [bbTBA] with either 4 or 300 µM Ca^{2+}. For activation with 4 µM Ca^{2+} (Fig. 13 A), even with 20 µM bbTBA (which produces a >50% reduction in tail current amplitude measured at −150 mV), there is little discernible effect on tail current time course (Fig. 13, B and C), consistent with earlier observations (Wilkens and Aldrich, 2006). However, with 300 µM Ca^{2+} (Fig. 13 D), both 5 and 20 µM bbTBA exhibited clear effects on tail current behavior, producing both a slowing of tail current decay and a slight unblocking hook at the beginning of the tail current (Fig. 13 E). The slowing of the tail current decay was similar both at 5 and 20 µM bbTBA (Fig. 13 F), although 20 µM bbTBA produces almost a 30% greater reduction in peak tail current than 5 µM bbTBA (Fig. 13 E). Although the unblocking relaxation may seem counterintuitive if blocked channels can close, such a relaxation is expected when return of blocked channels to open states occurs more rapidly than closure of open or blocked channels.

We next examined the predictions for tail current behavior for various blocking models (Fig. 14). For Scheme 2a, there is little discernible effect of blocker on tail current deactivation for currents activated with a nominal 4 µM Ca^{2+} (Fig. 14 B, 1) However, with 300 µM Ca^{2+} (Fig. 14 B, 2), Scheme 2a exhibits some slight slowing of deactivation along with a clear unblocking hook in the tail current at the highest effective [blocker]. Similar effects are observed for most models (Fig. 14, C–G). For activation at a nominal 4 µM Ca^{2+}, bbTBA

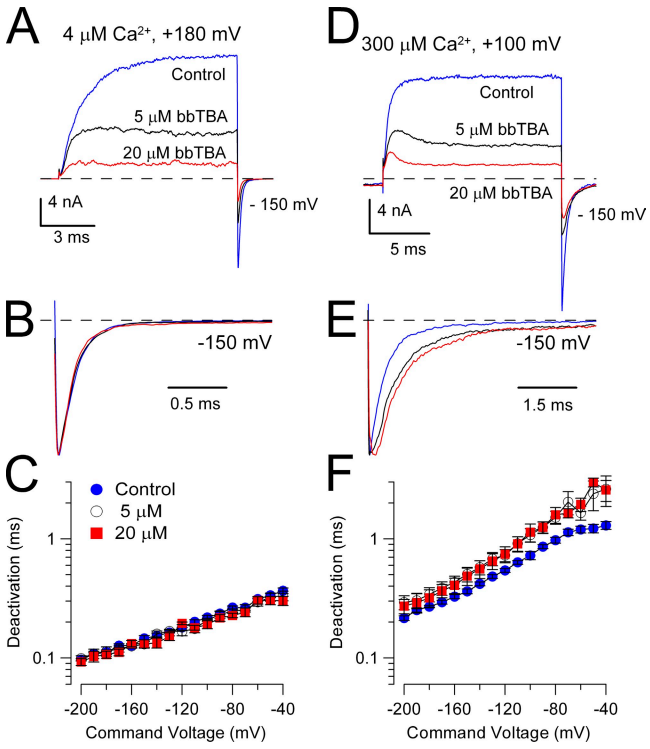

Figure 13. bbTBA causes slight tail current prolongation at higher Ca^{2+}, but not at 4 μM Ca^{2+}. (A) BK currents were activated by steps to +180 mV from a −100-mV holding potential with 4 μM of internal Ca^{2+}. Both 5 (black) and 20 μM (red) cause appreciable reduction both in outward current at +180 mV and tail current at −150 mV. (B) Tail currents in A were normalized to the peak tail current amplitude showing no difference in time course. (C) Deactivation time constants are plotted as a function of tail current potential for control and 5- and 20-μM bbTBA conditions. (D) Currents were activated by steps to +100 mV with 300 μM of internal Ca^{2+}, with tail current at −150 mV. (E) Tail currents in D were normalized to the peak current amplitude and the baseline for an exponential fitted to the decay phase, showing the slowing of deactivation and a slight hook of unblock in the current before deactivation. (F) The time constant of deactivation is plotted for the same three conditions as shown in C. The time constants in 5 and 20 μM bbTBA were indistinguishable from each other, but clearly were slowed relative to control time constants.

generally produces little effect on tail current decay, whereas for activation at 300 μM Ca^{2+}, there is typically more slowing of deactivation and a clear unblocking hook at the highest bbTBA concentrations. For the general Scheme 3a (Fig. 14 E), there is substantially more tail current prolongation predicted than for Scheme 2a, and some prolongation is observed, even at 4 μM Ca^{2+}. However, in all cases the magnitude of any slowing of tail current deactivation is rather minor. For Scheme 3b (Fig. 14 F), in which closed-channel block is voltage independent, no slowing of deactivation is observed at 4 μM. For the various models, we have plotted the deactivation time constant for tail current decay as a function of effective [blocker] (see Fig. S8). In most cases, blocker-dependent tail current prolongations observed in 300 μM Ca^{2+} exhibit saturation at the two highest [blocker], consistent with the similarity of tail current slowing produced by 5 and 20 μM bbTBA in native BK channels (Fig. 13).

The overall conclusion from this analysis is that several blocking models that incorporate block of closed channels do a reasonable job of approximating the observed lack of effect of bbTBA on tail currents with 4 μM Ca^{2+}, while reproducing the slight prolongation and tail current hook observed at 300 μM Ca^{2+}. As a consequence, we do not consider analysis of tail currents to be particularly useful in discriminating among the various models evaluated here.

DISCUSSION

The primary conclusion of this work is that the QA blocker, bbTBA, does not block BK channels in a completely state-independent fashion. The results generally support the conclusions of a previous study (Wilkens and Aldrich, 2006) indicating that bbTBA does block both open and closed BK channels. However, the difference with the earlier study is that here the results argue that bbTBA does not block BK channels in closed states with four inactive voltage sensors. We infer that voltage sensor movement is coupled to conformational changes in active-not-open channels that are permissive for block of closed channels by bbTBA. An important issue that we address below concerns the physical/structural basis by which closed channels with inactive voltage sensors are resistant to block by bbTBA.

bbTBA does not block BK channels by a completely state-independent mechanism

The simplest form of a fully state-independent blocking model (Scheme 2a) posits that both open and closed channels are blocked with equal affinity and voltage dependence. Our experiments present several observations inconsistent with this model. First, families of GV curves at different [bbTBA] obtained with either 100 or 300 μM Ca^{2+} are better fit with a strictly open-channel block model, whereas at 0 or 4 μM Ca^{2+}, GV curves are better fit with a CB–OB model. Second, our analysis of fractional unblock is not consistent with a completely state-independent mechanism of block. Third, although kinetic features of block by bbTBA support the existence of closed-channel block, the fractional availability of BK channels at negative potentials is inconsistent with a closed-channel block mechanism with voltage dependence similar to block of open channels. Fourth, and probably most directly, the results show that bbTBA does not reduce NPo at a potential at which voltage sensors are inactive. Collectively, these results exclude completely state-independent block by bbTBA.

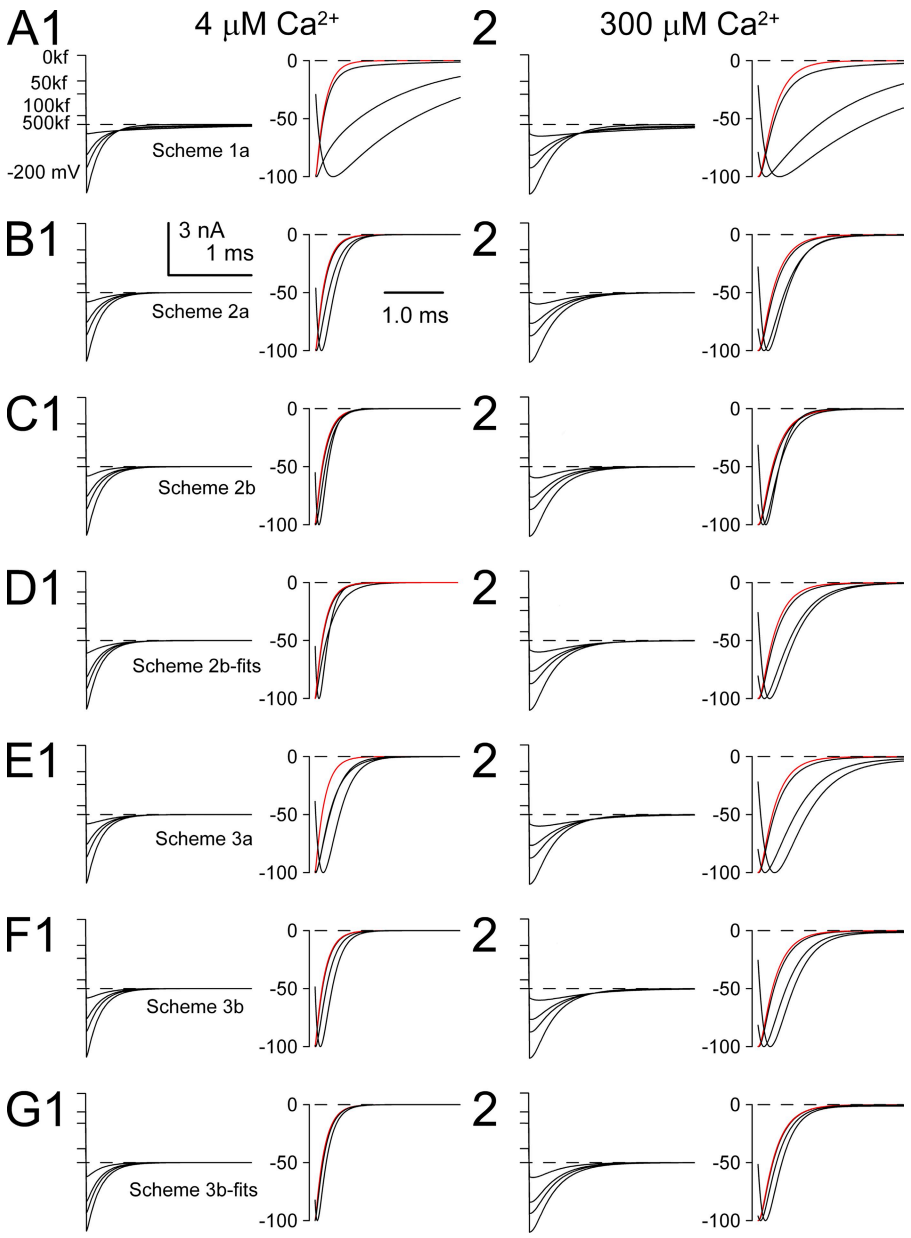

Figure 14. Absence of slowing of tail current deactivation is not strongly diagnostic among different versions of closed-channel block models. (A) Simulated tail currents were generated with Scheme 1a at −200 mV in the absence of blocker and then with effective 1×, 2×, and 10× increments of [blocker] (50, 100, and 500 kf) for both 4 μM Ca^{2+} (1) and 300 μM Ca^{2+} (2). At each concentration, sets of simulated traces show net current for 1,000 channels (left) and normalized tail currents (right). The trace in red highlights the normalized tail current in the absence of blocker. (B) Simulated tail currents are shown for Scheme 2a under the same conditions as in A. Note that for the highest [blocker] producing an almost 90% reduction in tail current amplitude, there is a noticeable unblocking hook, although changes in the time constant of deactivation are minimal. (C) Simulated tail currents are shown for Scheme 2b ($z_c = 0\ e$). There is minimal tail current prolongation and any unblocking hook is reduced compared with Scheme 2a. (D) Tail currents were simulated for a Scheme 2b′ model with parameters based on Fig. 4 F. (E) Tail currents were simulated with Scheme 3a. (F) Tail currents were generated with Scheme 3b. (G) Tail currents were simulated with Scheme 3b′ with parameters from the fit of the GV curve in Fig. 4 G.

The properties of fractional availability as a function of voltage are particularly revealing regarding the inadequacy of state-independent block. Fractional availability exhibits a fairly steep dependence on voltage along with saturation over negative potentials. These properties argue either that, at very negative potentials, fully closed channels are simply not blocked or that block of closed channels is voltage independent. However, neither of these interpretations is consistent with the fully state-independent block mechanism (Scheme 2a). On the contrary, our simulations clearly indicate that, if closed-state block shares a similar voltage dependence with open-state block, there should be an appreciable effect of closed-state block on fractional availability at potentials negative to −100 mV.

We also addressed whether the results might be explained by a form of Scheme 2 in which all open and closed channels can still be blocked by bbTBA, but open- and closed-channel block differ. We considered models in which closed-channel block is voltage independent ($z_c = 0.0\ e$; Scheme 2b) or all block parameters varied independently (Scheme 2′). With $z_c = 0.0\ e$, the triphasic relaxations in the current time course are not predicted. Furthermore, Scheme 2b is unable to account for the disparities in block by bbTBA between low and high Ca^{2+} (Fig. 3 B), and does not provide adequate fits of GV curves at low and high Ca^{2+} (Fig. 4 F). This inability of Scheme 2b to account for the observations holds even when $K_{bc} \neq K_{bo}$. For Scheme 2′, the optimal fit required that z_c is ∼0.8 *e*, which predicts

unusual channel kinetic behavior because of a large change in the effective gating charge in the CB–OB transitions (Fig. S8). Based on the inability of any form of Scheme 2 to describe several important features of block by bbTBA, we propose that the absence of appreciable change in fractional block of BK channels over holding potentials from −100 to −300 mV indicates that the fully closed BK channel is not blocked by bbTBA. This conclusion is also directly supported by the apparent absence of a reduction in NPo by 100 µM bbTBA at −150 mV. However, a complication in the measurement of NPo was that 100 µM bbTBA produced a small net increase in NPo, an effect not predicted by any blocking scheme. This effect complicates interpretation of the absence of any blocking effect because one might argue that a blocking effect is being masked by the simultaneous increase in NPo. However, we calculate that, if the observed increase in NPo is masking a block effect of this magnitude, it would require an over 10-fold increase in NPo, an increase we consider unlikely. At 30 µM Ca^{2+}, the Ca^{2+} activation machinery is already strongly activated (Horrigan and Aldrich, 2002). Furthermore, we know of no other known allosteric regulator pathways of BK channels, e.g., Mg^{2+} (Horrigan and Ma, 2008), that might produce increases in NPo of this magnitude. Finally, if 100 µM bbTBA were causing strong allosteric activation of BK channels at −150 mV, one might also expect this activation to also occur at +20 mV. If that were the case and bbTBA was also blocking BK channels in a completely state-independent fashion, we would have expected to see similar reductions in NPo both at −150 and +20 mV. This is not observed. Thus, the absence of any reduction in NPo at −150 mV with 100 µM bbTBA is best explained by the idea that block by bbTBA at −150 mV is much less than at +20 mV. Although it will be important to identify the basis for the increase in NPo observed with bbTBA, at present the results seem best explained by the idea that bbTBA does not block channels with inactive voltage sensors, but that the quaternary bbTBA also produces some small increase in NPo through some unidentified, perhaps electrostatic effect.

Where our results lead to different conclusions than the earlier observations of Wilkens and Aldrich (2006), it is primarily because the conditions over which block by bbTBA was examined in the present study were extended, either by examination of low and high Ca^{2+} or by the use of more negative voltages. Both studies support the view that bbTBA does block closed BK channels, but the present results find that channels with inactive voltage sensors appear insensitive to bbTBA block. Thus, in comparing different blocking models, it is critical that conditions must be identified over which measurable model-dependent differences are expected.

What is the correct blocking model?

Our results argue that closed BK channels with inactive voltage sensors are resistant to block by bbTBA and support the idea that voltage-dependent conformational changes occurring in closed channels are permissive for bbTBA block. These conclusions do not depend on any particular model of channel block. However, a major part of this work involved an attempt to distinguish among different channel block models in which block was coupled to voltage sensor movement. For BK channels, voltage sensor movement both in closed and open channels is very rapid relative to channel opening and closing conformational changes (Horrigan and Aldrich, 1999, 2002). Therefore, after a voltage step, at least some voltage sensors will be rapidly activated at any Ca^{2+} concentration, perhaps producing a conformational change sufficient to permit block of closed channels. We focused our evaluation of models in which block was coupled to movement of voltage sensors on Scheme 3, in which activation of a single voltage sensor was considered sufficient to confer full sensitivity of a closed channel to block. Although we have not presented detailed examples, we also considered a Scheme 4 (Fig. S4), in which block affinity scaled linearly with the number of active voltage sensors. Both models were able to account for many essential features of the data, including the differences in block by bbTBA at low and high Ca^{2+}, the fractional availability curves, and also fractional unblock curves. However, because Scheme 4 was not obviously superior to Scheme 3 and any choice for how block affinity may scale with voltage sensor movement is rather arbitrary, we have omitted detailed consideration of Scheme 4.

We have also given consideration to several other possibilities. These include: (1) that perhaps block of the central cavity only occurs when at least two voltage sensors are active (Table III; Scheme 6); (2) that block of closed channels scales with voltage sensor movement, but not block of open channels (Table III, Scheme 5); and (3) that the closed-channel blocking affinity increases in a superlinear fashion with the number of active voltage sensors up to some limit. The available data do not discriminate adequately among different variations of closed-channel block coupled to active voltage sensors, and we have not extensively evaluated the behavior of these alternative models. We also considered and excluded a two-site blocking model (see Materials and methods), one site corresponding to open-channel block and a second site accessible in both open and closed states.

Although schemes based on the coupling of block to voltage sensor movement (such as Scheme 3) can account for many aspects of block by bbTBA, neither Scheme 3 nor other variations of schemes in which block depends on voltage sensor movement provide an optimal description of block of BK channels by bbTBA.

TABLE III

Model-dependent parameters resulting from fit of GV curves

Basic open-channel block				
Scheme 1	Scheme 1a			
K_{bo} (μM)	5.90 ± 0.40			
z_c	0.13 ± 0.02 *e*			
K_{bc} (μM)				
z_c				
SSQ	395.95			
State-independent closed- and open-channel block and variations				
Scheme 2	Scheme 2a	Scheme 2a′	Scheme 2b	Scheme 2b′
K_{bo} (μM)	7.42 ± 0.43	6.01 ± 0.30	6.96 ± 0.39	6.36 ± 0.45
z_c	0.17 ± 0.02 *e*	0.10 ± 0.02 *e*	0.15 ± 0.2 *e*	0.15 ± 0.02 *e*
K_{bc} (μM)	$=K_{bo}$	45.79 ± 35.9	$=K_{bo}$	21.4 ± 12.2
z_c	$=z_c$	0.81 ± 0.20 *e*	0.0*	0.0*
SSQ	309.199	100.66	486.663	326.09
Block dependent on movement of one voltage sensor				
Scheme 3	Scheme 3a	Scheme 3a′	Scheme 3b	Scheme 3b′
K_{bo} (μM)	6.14 ± 0.26	6.01 ± 0.27	6.02 ± 0.29	6.48 ± 0.29
z_o	0.13 ± 0.01 *e*	0.10 ± 0.02 *e*	0.13 ± 0.02 *e*	0.13 ± 0.01 *e*
K_{bc} (μM)	$=K_{bo}$	8.1 ± 6.7	$=K_{bo}$	2.34 ± 0.38
z_c	$=z_c$	0.44 ± 0.23 *e*	0.0	0.0*
SSQ	159.163	93.75	209.18	138.242
Block scales with movement of each voltage sensor				
Scheme 4		Scheme 4a′		Scheme 4b′
4 K_{bo} (μM)		19.53 ± 0.9		20.78 ± 0.80
z_o		0.06 ± 0.02 *e*		0.08 ± 0.01 *e*
4 K_{bc} (μM)		7.4 ± 5.2		3.05 ± 0.44
z_c		0.30 ± 0.21 *e*		0.0*
SSQ		90.3005		106.822
Closed-channel block scales with movement of each voltage sensor; open channels are blocked identically				
Scheme 5		Scheme 5a′		Scheme 5b′
K_{bo} (μM)		6.03 ± 0.28		6.38 ± 0.26
z_o		0.10 ± 0.02 *e*		0.12 ± 0.01 *e*
4 K_{bc} (μM)		8.52 ± 6.4		3.21 ± 0.48
z_c		0.33 ± 0.23 *e*		0.0*
SSQ		95.99		121.019
Closed channel block depends on movement of two voltage sensors				
Scheme 6		Scheme 6a′		Scheme 6b′
K_{bo} (μM)		6.04 ± 0.24		5.70 ± 0.23
z_o		0.10 ± 0.02 *e*		0.069 ± 0.01 *e*
4 K_{bc} (μM)		0.02 ± 0.02		.174 ± 0.02
z_c		0.62 ± 0.23 *e*		0.0*
SSQ		89.91		124.9026

At present, we simply interpret the analysis as supportive of the idea that block of closed BK channels depends on activation of one or more voltage sensors. Models that include this idea allow fitting of bbTBA block of GV curves at both low and high Ca^{2+}, and can account for the Po independence of fractional unblock by bbTBA, the fractional availability of channels in bbTBA as a function of voltage, the kinetic aspects of block by bbTBA, features of tail current alteration by bbTBA, and the absence of blocking effects of bbTBA on NPo at negative potentials.

Conceptualizing the physical basis for dependence of closed-channel block on voltage sensor movement

Accepting the view that closed-channel block only occurs subsequent to movement of at least one voltage sensor, the key question that arises is, What is the physical change in the channel that allows blockade by bbTBA once a voltage sensor moves? Our results provide no specific answer to this question. As noted at the beginning of the Results, we envision two primary types of explanation, both of which assume that the bbTBA-binding site is within the BK central cavity: first, a change

in bbTBA accessibility to the central cavity and, second, a change in bbTBA binding affinity within the central cavity. In one case, movement of the voltage sensor is imagined to link to other elements of the pore domain to allow access of bbTBA to a central cavity binding site. In the other, the voltage sensor movement results in a change within the central cavity that increases the bbTBA binding affinity.

The idea that access of bbTBA to the central pathway changes with voltage sensor movement supposes that movement of the voltage sensor, in association with movement of the S4-S5 linker, also results in displacement of the S6 inner helix from its resting position, thereby creating a pathway of access to the central cavity. Thus, in the fully resting condition, the aperture to the central cavity would be sufficiently small to prevent bbTBA access, although perhaps allowing entry of smaller molecules, including permeant ions. Subsequently, the rapid movement of BK voltage sensors, which markedly precedes BK channel activation (Horrigan and Aldrich, 1999, 2002), might lead to an increase in diameter of the aperture, effectively allowing bbTBA to enter the still-closed channel. The actual opening of the BK channel permeation pathway would then involve movement of a gate located elsewhere, presumably at the selectivity filter as suggested by Wilkens and Aldrich (2006).

The idea that a portion of the inner helix of K^+ channels can move in a not-yet-open channel has been supported by experiments on the *Shaker* K^+ channel by del Camino et al. (2005), who exploited a construct in which the voltage dependence of voltage sensor movement is markedly shifted leftward of the channel-opening equilibrium. This allowed identification of inner helix residues that became accessible in closed channels with activated voltage sensors (activated-not-open channels), but which were not accessible in closed or open states, supporting the idea that inner helix movement in K^+ channels may occur in conjunction with voltage sensor movement in the absence of channel openings. Here, for BK channels, in accordance with this explanation of bbTBA block, any rearrangement of the inner helices that may occur upon voltage sensor activation must be sufficient to allow access to the channel central cavity, even while channels remain closed. Given the molecular dimensions of bbTBA, accessibility to the central cavity in a closed channel would imply that a fairly large access path to the central cavity is created upon movement of perhaps a single voltage sensor. Any blocking molecules smaller than bbTBA would be expected to have even more ready access to the central cavity in activated-but-closed channels. In fact, the lack of effect of QA blockers on BK tail currents supports the idea that block of closed states of BK channels by a variety of QA blockers does occur (Li and Aldrich, 2004), although it leaves open the question of whether such compounds also block closed channels with inactive voltage sensors.

Properties of BK channel inactivation also support the idea that voltage-dependent conformational changes precede BK channel opening. At low open probabilities, inactivation of BK channels can occur in the absence of channel openings, consistent with the idea that there are voltage-dependent conformational changes among closed BK channel states that are permissive for the inactivation domains of BK β2 subunits to reach a position of block (Ding and Lingle, 2002). Collectively, these results support the idea that voltage-dependent changes in aperture dimension may occur in BK channels in the absence of overt channel opening.

The idea that there are changes in dimension at the cytosolic end of the BK inner helix during gating is also supported by work with the *Shaker*B N-terminal peptide (Li and Aldrich, 2006). In contrast to bbTBA and tetrabutylammonium, the ShakerB peptide produces a state-dependent block of BK channels that is also associated with a hindering of channel closing during deactivation (Li and Aldrich, 2006). Li and Aldrich proposed that the differences in behavior of BP and bbTBA arise from the idea that the aperture to the central cavity in closed channels is simply too small to allow passage of the larger BP molecule, while permitting entry of bbTBA.

An alternative explanation for the absence of bbTBA block in closed states with inactive voltage sensors is that perhaps the affinity for bbTBA differs between closed channels with resting or active voltage sensors. To our knowledge, whether binding affinity within the central cavity may change between open and closed states has not been addressed for any K^+ channel. Among different K^+ channels, block by internal TEA exhibits a wide range of open-state affinities, despite the assumed similarity of architecture at the entrance of K^+ channel selectivity filters. For example, estimates of 0-voltage TEA binding affinity include ~75 mM for Kcsa (Kutluay et al., 2005), 0.56 mM for *Shaker* (Thompson and Begenisich, 2000), and 25 mM for BK channels (Yellen, 1984). Given differences in the blocking affinities of cytosolic TEA among different open K^+ channels, it might not be surprising that in association with channel gating, there are also changes in the central cavity or vicinity of the selectivity filter that might influence TEA affinity. However, for a bulky blocker like bbTBA, the determinants of binding are likely to be different than for TEA. In *Shaker*, residues in the P loop near the selectivity filter have been shown to influence affinity for block by smaller QA blockers, whereas the affinity of block by QA blockers with long hydrophobic side chains is affected by mutations at hydrophobic residues in S6 (Choi et al., 1993). If bbTBA binding affinity differs among different closed states, it would suggest that voltage sensor movement is causing a change in the strength of hydrophobic interactions between bbTBA and central cavity residues.

Overall, the results provide no definitive basis for distinguishing between the access or affinity explanations. However, because of the precedent that conformational changes may occur at the cytosolic end of K^+ channels that are coupled to voltage sensor movement, we prefer the view that bbTBA gains access to the central cavity through expansion of an aperture that is sufficient to allow bbTBA passage as soon as at least one voltage sensor is active. We consider it less likely a change in strength of hydrophobic interactions within the central cavity might occur as a consequence of voltage sensor movement.

The above discussion leaves open the possibility that, even with four resting voltage sensors, an aperture of finite open dimension exists that allows molecules smaller than bbTBA to enter the central cavity. The gating behavior of BK channels and the allosteric model of BK activation that best accounts for this behavior implicitly support this possibility, at least for open channels with four resting voltage sensors. Specifically, at very negative potentials, where voltage sensors are almost entirely inactive, BK channels have a finite Po that exhibits a voltage dependence characteristic of the C–O equilibrium defined by the equilibrium constant, L (Horrigan and Aldrich, 2002). The fact that the residual Po is independent of the voltage dependence of the voltage sensor equilibrium requires that the openings at negative potentials occur in channels in which voltage sensors are usually inactive. This necessarily suggests that permeant ions enter the central cavity and permeate through channels with four inactive voltage sensors. However, this separation of Po and voltage sensor activation does not directly identify the position of the gate(s) opened during the C to O transition. Openings that occur in the absence of voltage sensor activation might involve either of two mechanisms. First, perhaps in BK channels rearrangements of the S6 helices permitting ion access to the central cavity may occur independently of movement of the S4-S5 linker typically thought to be involved in pore opening for Kv channels (Lu et al., 2002; Long et al., 2005). Second, it is possible that an aperture sufficiently large to allow hydrated K^+ to enter the central cavity is always present in all BK channel conformations, and that the observed openings simply reflect a gating process at the selectivity filter. The latter interpretation seems most consistent with our current understanding of steps in BK gating.

Considerations pertinent to the voltage dependence of closed-channel block

A final issue concerns the properties of closed-channel block and, in particular, the voltage dependence of closed-channel block, z_c. Given that bbTBA appears to block both open and closed channels, it would be desirable to know how the binding affinity and voltage dependence compares for open and closed states. However, no aspect of our data allows any model-independent estimate of the properties of closed-channel block, and our estimates of K_{bc} and z_c are based entirely on the use of simultaneous fitting of GV curves at both low and high Ca^{2+} to the various models. Although the simultaneous fitting is an advantage in parameter estimation, the GV curves cannot be considered to strongly define parameter values for closed-channel block because closed-channel block primarily contributes only at the foot of the GV curves. Yet, it is satisfying that the conclusion that closed-channel block depends on voltage sensor movement, based on our fitting of GV curves, was strongly and directly supported by measurements of NPo at negative potentials. This suggests that at least some aspects of closed-channel block can be reliably assessed by model-dependent fitting of the GV curves.

To ascertain properties of closed-channel block, we examined the ability of different blocking schemes (Schemes 2–4) to fit GV curves, under different assumptions regarding the relationship of K_{bc} and K_{bo}, as well as z_c and z_o. Under the most relaxed condition, when $K_{bc} \neq K_{bo}$ and both z_c and z_o were allowed to vary, the best fit to GV curves yielded values for z_c with large voltage dependence. However, a difficulty with large values of z_c is that, to maintain microscopic reversibility in tiered reaction schemes, strong allosteric effects on transitions between CB and OB states are required, and such effects were not observed. In contrast, although fits of GV curves with $z_c = z_o$ or $z_c = 0.0$ *e* were not quite as good, the weaker closed-state voltage dependence resulted in simulated currents that better approximate the observed BK current behavior. Yet, overall, for Scheme 3, the fits obtained either when z_c was allowed to vary or when $z_c = 0$ *e* were only slightly different, suggesting that one cannot draw strong conclusions based on different estimates of z_c. Furthermore, it should be noted that, regardless of the assumptions for z_c under different variations of Scheme 3 (Table III), K_{bo} and K_{bc}, the 0-voltage open- and closed-channel affinities for bbTBA are fairly similar, suggesting that the determinants for bbTBA binding are similar in open and closed channels.

Theoretical considerations have suggested that closed-channel block might be expected to exhibit stronger voltage dependence than open-channel block. Calculations based both on the crystal structure of the presumed closed KcsA channel and also on an open-state model indicate that substantial differences exist in the expected transmembrane potential drop along the channel axis (Roux et al., 2000). Specifically, at the level of the central cavity, a larger fraction of the total field (relative to the inside) is felt in closed channels ($z\delta$ of $\sim$0.46 *e*) versus open channels ($z\delta$ of $\sim$0.3 *e*), suggesting that a larger voltage dependence of block in closed channels is expected. This idea would seem to conflict with our observation that the assumption of $z_c > z_o$ can

result in predictions for kinetic aspects of currents that are not plausible. However, it should be kept in mind that the models we have evaluated make the assumption of microscopic reversibility in the coupling of blocking steps with gating steps. Thus, under this assumption, our analysis would argue that z_c is unlikely to be much larger than z_o. However, it may be the case that this assumption may not be necessary or entirely appropriate. For example, the effect of a voltage gradient acting on a charged moiety in the central cavity might provide energy that effectively introduces asymmetry into a block mechanism. Perhaps models in which $z_c > z_o$ and which allow deviations from microscopic reversibility might better account not only for the steady-state aspects of our results, but also for the various kinetic features of block. Despite the uncertainty on this point, these considerations do not negate our conclusion regarding the inability of bbTBA to block channels with four inactive voltage sensors.

Summary

The results and analysis support the view that bbTBA does not block BK channels in a completely state-independent fashion, but that blockade of closed channels is dependent on movement of at least one or more voltage sensors. In contrast to *Shaker* K^+ channels, in BK channels movements of the inner helix associated with voltage sensor movement allow blockers to gain access to the central cavity in the closed channel. The analysis does not define the physical mechanism that accounts for the inability of bbTBA to block closed channels with inactive voltage sensors, but we discuss two possibilities: that access to the central cavity depends on voltage sensor movement, or that bbTBA affinity in the central cavity is altered by voltage sensor movement.

We thank Yefei Cai for the handling of oocytes. Special thanks to Dr. J.A. De. Santiago-Castillo for modifications to IChSim.

This work was supported by GM 066215 to C.J. Lingle.

Christopher Miller served as editor.

Submitted: 28 April 2009
Accepted: 2 October 2009

REFERENCES

Armstrong, C.M. 1971. Interaction of tetraethylammonium ion derivatives with the potassium channels of giant axons. *J. Gen. Physiol.* 58:413–437. doi:10.1085/jgp.58.4.413

Armstrong, C.M., and B. Hille. 1972. The inner quaternary ammonium ion receptor in potassium channels of the node of Ranvier. *J. Gen. Physiol.* 59:388–400. doi:10.1085/jgp.59.4.388

Benzinger, G.R., X.M. Xia, and C.J. Lingle. 2006. Direct observation of a preinactivated, open state in BK channels with β2 subunits. *J. Gen. Physiol.* 127:119–131. doi:10.1085/jgp.200509425

Brelidze, T.I., and K.L. Magleby. 2005. Probing the geometry of the inner vestibule of BK channels with sugars. *J. Gen. Physiol.* 126:105–121. doi:10.1085/jgp.200509286

Choi, K.L., R.W. Aldrich, and G. Yellen. 1991. Tetraethylammonium blockade distinguishes two inactivation mechanisms in voltage-activated K^+ channels. *Proc. Natl. Acad. Sci. USA.* 88:5092–5095. doi:10.1073/pnas.88.12.5092

Choi, K.L., C. Mossman, J. Aubé, and G. Yellen. 1993. The internal quaternary ammonium receptor site of Shaker potassium channels. *Neuron.* 10:533–541. doi:10.1016/0896-6273(93)90340-W

Cui, J., and R.W. Aldrich. 2000. Allosteric linkage between voltage and Ca^{2+}-dependent activation of BK-type mslo1 K^+ channels. *Biochemistry.* 39:15612–15619. doi:10.1021/bi001509+

Cui, J., D.H. Cox, and R.W. Aldrich. 1997. Intrinsic voltage dependence and Ca^{2+} regulation of *mslo* large conductance Ca-activated K^+ channels. *J. Gen. Physiol.* 109:647–673. doi:10.1085/jgp.109.5.647

del Camino, D., and G. Yellen. 2001. Tight steric closure at the intracellular activation gate of a voltage-gated K^+ channel. *Neuron.* 32:649–656. doi:10.1016/S0896-6273(01)00487-1

del Camino, D., M. Kanevsky, and G. Yellen. 2005. Status of the intracellular gate in the activated-not-open state of shaker K^+ channels. *J. Gen. Physiol.* 126:419–428. doi:10.1085/jgp.200509385

Demo, S.D., and G. Yellen. 1991. The inactivation gate of the Shaker K^+ channel behaves like an open-channel blocker. *Neuron.* 7:743–753. doi:10.1016/0896-6273(91)90277-7

Ding, J.P., and C.J. Lingle. 2002. Steady-state and closed-state inactivation properties of inactivating BK channels. *Biophys. J.* 82:2448–2465. doi:10.1016/S0006-3495(02)75588-4

Hamill, O.P., A. Marty, E. Neher, B. Sakmann, and F.J. Sigworth. 1981. Improved patch-clamp techniques for high-resolution current recording from cells and cell-free membrane patches. *Pflugers Arch.* 391:85–100. doi:10.1007/BF00656997

Heginbotham, L., and E. Kutluay. 2004. Revisiting voltage-dependent relief of block in ion channels: a mechanism independent of punchthrough. *Biophys. J.* 86:3663–3670. doi:10.1529/biophysj.103.039412

Horrigan, F.T., and R.W. Aldrich. 1999. Allosteric voltage gating of potassium channels II: mSlo channel gating charge movement in the absence of Ca^{2+}. *J. Gen. Physiol.* 114:305–336. doi:10.1085/jgp.114.2.305

Horrigan, F.T., and R.W. Aldrich. 2002. Coupling between voltage sensor activation, Ca^{2+} binding and channel opening in large conductance (BK) potassium channels. *J. Gen. Physiol.* 120:267–305. doi:10.1085/jgp.20028605

Horrigan, F.T., and Z. Ma. 2008. Mg^{2+} enhances voltage sensor/gate coupling in BK channels. *J. Gen. Physiol.* 131:13–32. doi:10.1085/jgp.200709877

Horrigan, F.T., J. Cui, and R.W. Aldrich. 1999. Allosteric voltage gating of potassium channels I: mSlo ionic currents in the absence of Ca^{2+}. *J. Gen. Physiol.* 114:277–304. doi:10.1085/jgp.114.2.277

Jiang, Y., A. Lee, J. Chen, M. Cadene, B.T. Chait, and R. MacKinnon. 2002. Crystal structure and mechanism of a calcium-gated potassium channel. *Nature.* 417:515–522. doi:10.1038/417515a

Kutluay, E., B. Roux, and L. Heginbotham. 2005. Rapid intracellular TEA block of the KcsA potassium channel. *Biophys. J.* 88:1018–1029. doi:10.1529/biophysj.104.052043

Li, W., and R.W. Aldrich. 2004. Unique inner pore properties of BK channels revealed by quaternary ammonium block. *J. Gen. Physiol.* 124:43–57. doi:10.1085/jgp.200409067

Li, W., and R.W. Aldrich. 2006. State-dependent block of BK channels by synthesized shaker ball peptides. *J. Gen. Physiol.* 128:423–441. doi:10.1085/jgp.200609521

Lingle, C. 1983. Blockade of cholinergic channels by chlorisondamine on a crustacean muscle. *J. Physiol.* 339:395–417.

Lingle, C.J., X.-H. Zeng, J.-P. Ding, and X.-M. Xia. 2001. Inactivation of BK channels mediated by the NH_2 terminus of the β3b auxiliary subunit involves a two-step mechanism: possible separation of binding and blockade. *J. Gen. Physiol.* 117:583–606. doi:10.1085/jgp.117.6.583

Liu, Y., M. Holmgren, M.E. Jurman, and G. Yellen. 1997. Gated access to the pore of a voltage-dependent K+ channel. *Neuron.* 19:175–184. doi:10.1016/S0896-6273(00)80357-8

Long, S.B., E.B. Campbell, and R. Mackinnon. 2005. Voltage sensor of Kv1.2: structural basis of electromechanical coupling. *Science.* 309:903–908. doi:10.1126/science.1116270

Lu, Z., A.M. Klem, and Y. Ramu. 2002. Coupling between voltage sensors and activation gate in voltage-gated K^+ channels. *J. Gen. Physiol.* 120:663–676. doi:10.1085/jgp.20028696

Murrell-Lagnado, R.D., and R.W. Aldrich. 1993. Interactions of amino terminal domains of Shaker K channels with a pore blocking site studied with synthetic peptides. *J. Gen. Physiol.* 102:949–975. doi:10.1085/jgp.102.6.949

Neely, A., and C.J. Lingle. 1986. Trapping of an open-channel blocker at the frog neuromuscular acetylcholine channel. *Biophys. J.* 50:981–986. doi:10.1016/S0006-3495(86)83538-X

Neyton, J. 1996. A Ba^{2+} chelator suppresses long shut events in fully activated high-conductance $Ca^{(2+)}$-dependent K^+ channels. *Biophys. J.* 71:220–226. doi:10.1016/S0006-3495(96)79218-4

Rettig, J., S.H. Heinemann, F. Wunder, C. Lorra, D.N. Parcej, J.O. Dolly, and O. Pongs. 1994. Inactivation properties of voltage-gated K^+ channels altered by presence of beta-subunit. *Nature.* 369:289–294. doi:10.1038/369289a0

Roux, B., S. Bernèche, and W. Im. 2000. Ion channels, permeation, and electrostatics: insight into the function of KcsA. *Biochemistry.* 39:13295–13306. doi:10.1021/bi001567v

Ruppersberg, J.P., R. Frank, O. Pongs, and M. Stocker. 1991. Cloned neuronal IK(A) channels reopen during recovery from inactivation. *Nature.* 353:657–660. doi:10.1038/353657a0

Solaro, C.R., J.P. Ding, Z.W. Li, and C.J. Lingle. 1997. The cytosolic inactivation domains of BK_{Ca} channels in rat chromaffin cells do not behave like simple, open-channel blockers. *Biophys. J.* 73:819–830. doi:10.1016/S0006-3495(97)78114-1

Thompson, J., and T. Begenisich. 2000. Interaction between quaternary ammonium ions in the pore of potassium channels. Evidence against an electrostatic repulsion mechanism. *J. Gen. Physiol.* 115:769–782. doi:10.1085/jgp.115.6.769

Wei, A., C. Solaro, C. Lingle, and L. Salkoff. 1994. Calcium sensitivity of BK-type KCa channels determined by a separable domain. *Neuron.* 13:671–681. doi:10.1016/0896-6273(94)90034-5

Wilkens, C.M., and R.W. Aldrich. 2006. State-independent block of BK channels by an intracellular quaternary ammonium. *J. Gen. Physiol.* 128:347–364. doi:10.1085/jgp.200609579

Xia, X.M., J.P. Ding, and C.J. Lingle. 1999. Molecular basis for the inactivation of Ca^{2+}- and voltage-dependent BK channels in adrenal chromaffin cells and rat insulinoma tumor cells. *J. Neurosci.* 19:5255–5264.

Xia, X.M., X.-H. Zeng, and C.J. Lingle. 2002. Multiple regulatory sites in large-conductance calcium-activated potassium channels. *Nature.* 418:880–884. doi:10.1038/nature00956

Yellen, G. 1984. Ionic permeation and blockade in Ca2+-activated K+ channels of bovine chromaffin cells. *J. Gen. Physiol.* 84:157–186. doi:10.1085/jgp.84.2.157

Zeng, X.-H., X.-M. Xia, and C.J. Lingle. 2003. Redox-sensitive extracellular gates formed by auxiliary beta subunits of calcium-activated potassium channels. *Nat. Struct. Biol.* 10:448–454. doi:10.1038/nsb932

Zhang, X., C.R. Solaro, and C.J. Lingle. 2001. Allosteric regulation of BK channel gating by Ca^{2+} and Mg^{2+} through a nonselective, low affinity divalent cation site. *J. Gen. Physiol.* 118:607–636. doi:10.1085/jgp.118.5.607

Zhang, X., X.-H. Zeng, and C.J. Lingle. 2006. Slo3 K^+ channels: voltage and pH dependence of macroscopic currents. *J. Gen. Physiol.* 128:317–336. doi:10.1085/jgp.200609552

Zhou, M., J.H. Morais-Cabral, S. Mann, and R. MacKinnon. 2001. Potassium channel receptor site for the inactivation gate and quaternary amine inhibitors. *Nature.* 411:657–661. doi:10.1038/35079500